Lund University
Faculty of Science

Raman spectroscopy for characterization of soot and other carbonaceous materials

Jonatan Henriksson

Thesis submitted for degree of Master of Science
Project duration: 9 months

Supervised by Thi Kim Cuong Le and Per-Erik Bengtsson

Department of Physics
Division of Combustion Physics
May 2019

Abstract

Raman spectroscopy is well known as a method that can be used to study the structural characteristics of carbon materials such as soot and carbon black. In this work, a Raman spectroscopy setup was used to record spectra of various carbonaceous samples under different experimental conditions. The wave-number range of interest was from 900 to 3300 cm^{-1}, which includes the first and second order Raman peaks of carbonaceous materials. In addition to the Raman spectral features a fluorescence background was observed, which could be related to organic compounds including polycyclic aromatic hydrocarbons. The recorded spectra were analyzed using different deconvolution protocols to identify contributions from various spectral features relating to soot nanostructure. These deconvolution protocols were compared in terms of goodness-of-fit parameters. Furthermore, the influence of the laser radiation on spectral features was studied. Thus, the intensity variation of Raman and fluorescence signal were measured as function of laser power and exposure time, and the depolarization ratio for the primary peaks were estimated. The effects of heating the soot were studied from room temperature to 800 °C in air to obtain information regarding soot oxidation. The study has shown that Raman spectroscopy is a useful technique for structural characterization of soot and carbon black via their vibrational modes. Also, it was shown that care must be taken in experimental planning since parameters such as laser intensity and ambient conditions may influence the resulting data.

Contents

List of acronyms

- **BWF** Breit-Wigner-Fano
- **ELS** Elastic Light Scattering
- **FWHM** Full Width at Half Maximum
- **GoF** Goodness of Fit
- **HACA** Hydrogen-Abstraction-Carbon-Addition
- **HRTEM** High Resolution Transmission Electron Microscopy
- **HWHM** Half Width at Half Maximum
- **LIF** Laser Induced Fluorescence
- **LII** Laser Induced Incandescence
- **NOC** Nano-scale Organic Carbon
- **NRMSE** Normalized Root Mean Square
- **OP** Operation Point
- **PAH** Polycyclic Aromatic Hydrocarbon
- **STSA** Statistical Thickness Surface Area
- **TEM** Transmission Electron Microscopy

1 Introduction

Soot is formed through incomplete combustion of hydrocarbons while other similar carbonaceous materials can be produced under controlled incomplete combustion. Soot particles are comprised primarily of carbon, hydrogen and contain small amounts of other elements such as oxygen and nitrogen. The size of these primary particles is generally on the order of nanometers, and they aggregate to form larger structures containing tens to hundreds of primary particles [1, 2]. The properties of soot are of importance in different fields. For environmental research the behavior of soot particles in the atmosphere is a part of modelling atmospheric heating [2, 3]. Industrial applications of soot-like materials can be both wanted or unwanted, and are manufactured in some cases while in others it occurs as a byproduct. In combustion physics, soot is a component present in rich flames and is either the main focus of study or an influence on measurements not relating to soot specifically.

Soot is primarily studied in atmospheric sciences due to its contributions to heating of the atmosphere and its impact on human health [3]. As radiative forcing depends on optical properties of the particles, it is beneficial to have a well-developed understanding of the particles to accurately model their contribution [1, 2]. However, soot optical properties vary significantly depending on its formation process, size, morphology and chemical composition [3–5]. As a result, assumptions are often made regarding the absorption as function of wavelength in order to produce models, while in reality the optical properties of immature soot and mature soot can vary significantly [3]. To improve modelling, the formation of different types of carbonaceous materials and the resulting optical properties are beneficial to describe. The relation between optical properties and formation of these particles originates from particle structure on scales ranging from nanometer to micrometer scale [3, 6]. In terms of health aspects, atmospheric soot and combustion particulates have been shown to be cytotoxic and are pollutants which can have adverse effects on the respiratory system of humans due to the chemical properties of the soot [1, 2, 7, 8].
An important group of molecules for soot formation is Polycyclic Aromatic Hydrocarbons (PAH) which are in the range between black carbons (high specific absorption) and colorless organics (low specific absorption) for the optical classification and between elemental carbon (high refractive organics) and non-refractory organics in the thermochemical classification [4]. PAHs are planar molecules consisting of aromatic rings with hydrogen atoms or other molecular groups at the edges. PAHs are viewed as precursors in soot formation and are also a constituent of soot particle structure. As described in section 2.1, PAHs coalesce into aromatic clusters which form a core-shell structure in soot particles.

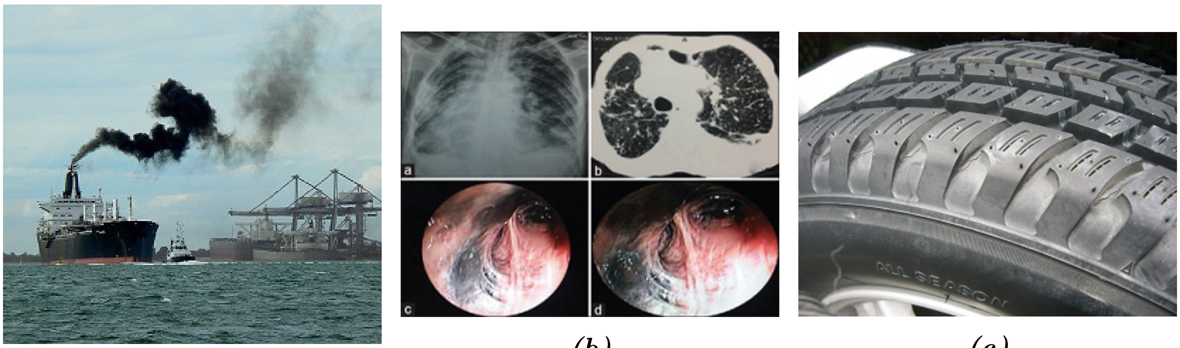

(a) (b) (c)

Figure 1: *(a) Soot emitted into the atmosphere affects the radiative transfer of the atmosphere and contributes to atmospheric heating [9]. (b) Lungs of a person that has inhaled soot, which has been shown to be carcinogenic [10]. (c) One application of carbon black is in tires, where it is blended with polymers to change the mechanical properties of the material [11, 12].*

A variety of carbon materials exist and their properties are related to their structure. Carbon occurs in the form of different allotropes, including graphite and diamond. Single crystal graphite consists of stacked graphene layers, which in turn are composed of planar aromatic rings of six carbon atoms. Diamond on the other hand consists of a tetrahedrally oriented lattice of carbon atoms. The optical and mechanical properties of these allotropes are then a result of the ordering of the atomic lattices. In contrast to these allotropes, amorphous carbon materials are unordered materials which lack crystalline structure [13]. These materials can be described in terms of the distribution of hybridization states, which is described in section 2.2 of this thesis.

Industrial applications for carbonaceous materials are for example carbon black, which is a type of material used for ink pigment, rubber filler and UV reinforcement of plastics [12]. Carbon black is produced from incomplete combustion similarly to soot and has similar structure; however carbon black is formed under controlled conditions. As a result, the material can be produced with specific properties, such as surface area to volume ratio and morphology.

Methods that have been used for the purpose of studying soot include structural and constituent based techniques such as X-ray techniques, Transmission Electron Microscopy (TEM) and mass spectroscopy, while various other optical techniques are used to study the behavior in flames [4, 14–16]. X-ray diffraction is used to study periodic structures and morphology, having the benefit of determination of the presence of specific structures such as fullerenes or nanotubes [1, 2]. TEM is an imaging technique based on electron transmission and provides images with up to nanometer resolution that reveal the morphology of soot primary particles and aggregates. As TEM provides images of the internal structure, determination of cluster sizes and distances can be performed. TEM can also provide an overview of the structural changes between different regions of the soot particles [14, 17]. Both X-ray diffraction and TEM provide structural information that relates to information obtained from Raman methods and often these are used in conjuncture to obtain comprehensive information. Mass spectroscopy, primarily photoionization mass spectroscopy, has been used to study the composition of soot [18]. Using mass spectroscopy, the mass of nascent soot particles or precursor molecules at different stages of the formation process has been determined for different types of flame conditions [19, 20]. Notably, the presence of PAH clusters was determined from higher mass particles observed in PAH measurements using mass spectroscopy [18].

To study the behavior of soot in flames and its optical properties, methods using Laser Induced Incandescence (LII), Elastic Light Scattering (ELS), Laser induced fluorescence (LIF), as well as UV and visible absorption have been successful [2, 16, 18, 21]. LII consists of laser heating of soot particles to produce incandescence. The incandescence signal can then be used to determine spatial distribution of particles and soot volume fraction through the use of temporal signal gating or particle sizes using time resolved signal detection. LII methods utilize from the high absorption of soot relative to other flame components to its benefit, so to selectively heat soot particles [22, 23]. ELS is, as the name suggests, based on scattering of light from soot particles [16, 23]. Primarily this is performed with laser light and the ELS signal is measured to indicate relative amount of soot particles and morphology [2]. LIF is the fluorescence which is produced when molecules are excited by incoming laser light [23] and is commonly used in combustion studies for spatial distribution of molecules such as PAH in flames [18]. LII, ELS and LIF have been performed on specific flames [2, 16, 22, 24], which gives a detailed description of the soot behavior from distribution in the flame down to the soot aggregate size and precursor molecules. PAH molecules also have strong absorption in the UV, and UV absorption can be used to study the aromaticity of PAHs, as the amount of aromatic rings shifts the absorption bands [2, 21].

In this thesis the method of study is Raman spectroscopy, which allows study of nanoscale structures in samples. Raman spectroscopy is an inelastic scattering technique and will be described in detail in section 2.3.1. The benefit of using Raman spectroscopy in the case of carbon-based solids is that lattice vibrations are probed, which provides information regarding the crystalline or amorphous structures. For soot particles the sizes of the crystalline domains and structural disorder contribute to the band structure, which in turn relates to the optical properties [25–27]. Using Raman spectroscopy, the structure of different samples of carbonaceous materials was probed under different conditions, such as temperature, manufacturing process, polarization of excitation laser and type of gas enveloping the sample during measurement.

2 Background

This section provides a short summary on the soot and carbon black formation process, structural properties, optical properties resulting from the structure and how structural information can be obtained from the Raman spectroscopy.

2.1 Formation of soot

Soot is formed in incomplete combustion through various pathways depending on fuel-air ratio, pressure, fuel and flame type. In fig.2 the formation process is illustrated along with TEM images of soot throughout the formation process. Its formation is a complicated process, occurring typically within a few milliseconds and includes two main stages; soot precursor formation and soot particle evolution. The transition between these two stages is called nucleation and is poorly understood [18]. The dominant theory is that soot nucleation begins with the appearance of PAHs that can nucleate into clusters of PAH molecules such as graphitic, fullerene-like and three dimensional cross-linked structures [28]. These PAH clusters, referred to as Nano-scale Organic Carbons (NOC) or nascent soot, grow by accumulating PAHs and carbon while in the flame. One of the primary pathways is the Hydrogen-Abstraction-Carbon-Addition (HACA) process which reduces the hydrogen to carbon ratio while increasing the size of the particle by addition of C_2H_2 [2, 28, 29]. Other processes also add to the growth process, such as methyl group additions [18]. As the soot particles grow the internal structure undergoes change as well. Initially the soot particle contains stochastically ordered PAH clusters and amorphous carbon regimes. The core of the particle remains primarily amorphous, however throughout the flame the outer PAH clusters organize through surface growth and annealing, resulting in a shell-like structure where clusters align in spherical layers with increasing similarity to graphite. These mature soot particles take on a core-shell structure, which contains amorphous and relatively ordered regions. These primary particles aggregate to form soot aggregates of tens to hundreds of primary particles [5].

Carbon black is a commercial product that has different applications and is manufactured by controlled incomplete combustion of hydrocarbon fuels, often PAH-rich fuels [12, 30]. The formation of carbon black is similar to that of soot in terms of aggregating PAHs and surface growth resulting in core-shell like structure, however the particles are

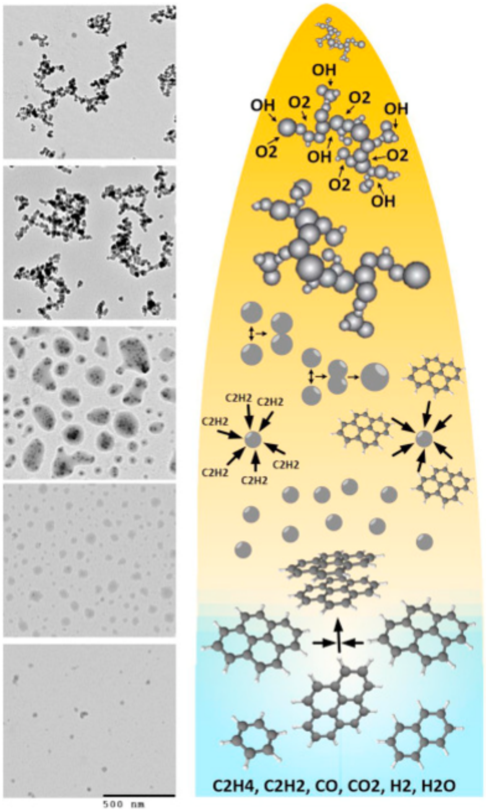

Figure 2: *An overview of soot formation in a flame as well as TEM images of soot particles from different stages of the process. The soot precursors (PAHs) form and begin to cluster, followed by soot growth through a variety of processes which increase the relative carbon content. At this point the primary particles begin to aggregate and form larger particles. [5]*

often heated in inert atmosphere after the flame in order to increase graphitization and reduce hydrogen content [31]. The primary characterization methods used in industry are based on techniques that determine surface area, color, structure (on the aggregate scale) and various chemical properties. As a measure of surface area two methods are used, nitrogen adsorption and iodine adsorption. Both methods rely on coating the carbon black particles with the given liquid or gas to then measure change in mass as the adsorbed mass is proportional to the surface area. Iodine number is then measured in mg/g of adsorbed iodine per mass of carbon black while nitrogen adsorption is approximated to a surface area per weight (m^2/g) under the assumption that the nitrogen layer is one atom thick. Surface area and chemical behavior is important in rubber and plastic applications as the ability to bind to polymers is affected by these factors [30].

2.2 Properties of carbonaceous materials

2.2.1 Structural properties

Hybridization of atomic orbitals occurs for example when an atoms electron configuration is such that bonds would require two external electrons to fill one orbital to fill the shell.

The electron configuration of carbon has two electrons in the 2s orbital and two 2p electrons, (1 p_x, 1 p_y, 0 p_z) for example. To fill the shell of carbon would then require four additional 2p electrons, however two of these would need to be placed in the same orbital (p_z in the aforementioned case). In terms of minimizing energy, it is then beneficial to excite one of the 2s electrons into the empty 2p orbital and allowing four covalent bonds. However, these bonds are now characterized by not only the 2p orbitals, but also the 2s orbital. In quantum mechanics, the combination of the s and p orbitals can be described by hybridization, where each hybrid orbital is a linear combination of one s and differing amounts of p orbitals [13]. Different allotropes of carbon such as diamond and graphite can be characterized by their hybridization state, where the sp^3 bond is a hybridization of the 2s orbital and three 2p orbitals, which produces a tetrahedral shape with four orbital lobes. This type of bond is characteristic of diamond, where all bonds are of the sp^3 type. If only two 2p orbitals are hybridized with the 2s orbital, it is called sp^2 hybridization which produces three orbital lobes in a plane, oriented with 120° degrees separation and a free standing 2p orbital (generally chosen to be p_z) perpendicular to the plane [13]. Graphene and therefore graphite, which is constructed from stacked layers of graphene, obtain their hexagonal structure from the sp^2 hybridization as this is the primary bond in these structures. The third hybridization state, sp hybridization, is not specific to any allotrope of carbon, but is present in carbon structures such as amorphous carbon and molecules such as acetylene (C_2H_2). sp hybridization combines the 2s orbital with one 2p orbital and is linear in structure [13].

Covalent bonds are separated into groups depending on the relative orientation of the overlapping orbitals and the two relevant types for sp^2 carbon are σ and π bonds [13]. σ bonds are formed when two orbitals are directly overlapping end-to-end. π bonds arise from side by side overlapping p orbitals that are parallel to each other [13]. In graphene, orbitals that are sp^2 hybridized bind with σ bonds while the single unhybridized p_z orbital binds with the surrounding p_z orbitals from other carbon atoms through π bonds. The importance of the π bonds for carbon materials such as graphene and graphite is that it is these π bonds that are responsible for conductivity in an otherwise non-metallic material. π bond electrons can move freely throughout the surface of the material even though other structures of carbon are not conductive, resulting in a semi-metal [13]. It has been shown in for examples ref. [32] that the band gap increases as the amount of aromatic rings decreases in a sp^2 bound carbon lattice, meaning soot or other carbonaceous materials containing nano-crystalline structures will have a non-zero band gap.

Soot contains all three hybridization states of carbon as a result of the stochastic formation process. PAHs consist of sp^2 hybridized carbon atoms but the various types of bonds between the polyaromatic clusters vary [2]. Nascent soot contains a relatively high fraction of sp^2 and sp^3 carbon, with limited amounts of sp hybridization in the form of cumulenic and polyynic structures. Generally, carbon that is a mixture of sp^2 and sp^3 hybridized carbon is referred to as amorphous carbon [2]. As the soot matures in the flame, the increasing carbonization and heating result in an increasingly sp^2 hybridization dominated material. This process can be called graphitization, as regions in the soot become increasingly similar to graphite in structure [1, 2, 13].

2.2.2 Optical properties

The optical properties of different carbonaceous substances can be understood in terms of extinction, which is the resulting loss of light intensity due to absorption and scattering in a sample [2]. The scattering cross-section depends primarily on morphology and size while absorption depends on the energy structure of the sample, for solids this relates to the energy band structure. Typical values of the optical band gap for soot range from 0.1 to 2.5 eV [27]. It is important to note that scattering also depends on band structure as well, as absorption leads to reduced scattered intensity [3]. Both scattering and absorption cross section are wavelength dependent and depending on the purpose of a study different parameters are important. For environmental application, the optical properties are necessary for understanding how soot particles interact with solar radiation [2]. This is often simulated using complex refractive index, which is related to the extinction coefficient, where Mie scattering, Rayleigh scattering and absorption are used to calculate atmospheric radiative transfer [3, 18]. The extinction coefficient describes attenuation of light passing through a medium. For soot the attenuation is dependent on wavelength and type of soot as the wavelength dependence of absorption changes with soot maturity [33].

2.3 Raman spectroscopy and its application to study carbonaceous materials

2.3.1 Raman spectroscopy

Raman spectroscopy is a spectroscopic technique based on Raman scattering, that probes vibronic energy structures in molecules and lattice vibrations in solids [34]. The Jablonski diagram shown in fig.3 displays the general processes of Rayleigh and Raman scattering in terms of energy levels. A system is excited to a virtual state by incoming radiation and for Rayleigh scattering the system de-excites to its original state. Raman scattering however, occurs when the system is de-excited to a different state and two types are defined, Stokes and anti-Stokes scattering where Stokes is red shifted and anti-Stokes is blue shifted. The Raman scattering process can be explained using different formalisms, however for this thesis the classical derivation will be used [35].

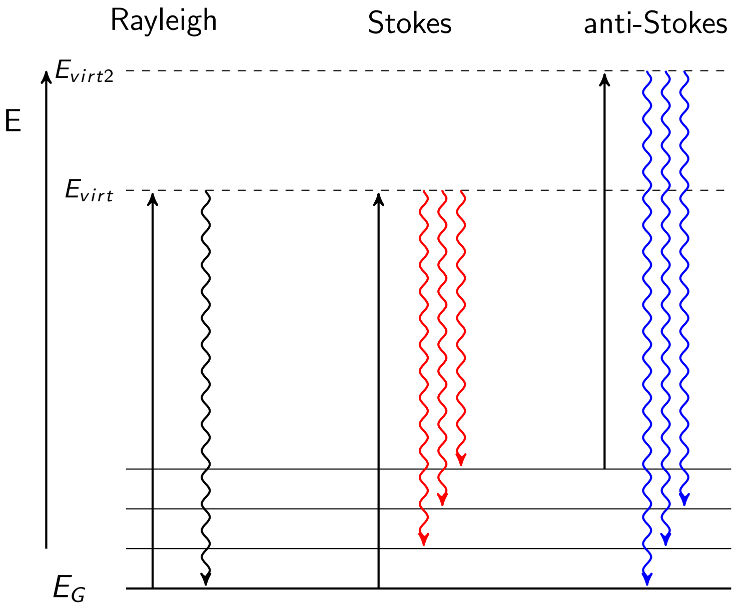

Figure 3: *Jablonski diagram displaying Rayleigh and Stokes and anti-Stokes Raman scattering. The system is excited to a virtual energy levels (E_{virt} or E_{virt2}) and for Rayleigh scattering the electron undergoes radiative de-excitation to the original state. Stokes scattering occurs when the electron is de-excited to a higher energy level, emitting a photon with less energy than the excitation photon. For anti-Stokes Raman scattering the photon excites an electron in a higher energy level and the emitted photon has more energy as a result of the electron de-exciting to a lower energy state*

Classically, it is necessary for a molecule to obtain an induced dipole moment to emit light. For this to occur there needs to be a displacement of charge and in the case of Raman scattering [34], it is the electron cloud that can become polarized by external fields. For a specific vibrational or rotational state to be Raman active, the rotation or vibration is required to have a variation in polarizability throughout the motion. Expressing the induced dipole moment P as a function of an external oscillating field E is done as follows:

$$\vec{P} = \alpha \vec{E} \tag{1}$$

$$\vec{E} = E_0 \cos\left(2\pi\nu_0 t\right) \tag{2}$$

where α is the polarizability of the molecule and ν_0 is the frequency of the external electric field. To express the polarizability as a function of the atomic motion, a simple model utilizes an oscillating homonuclear diatomic molecule where the displacement Q can be expressed as:

$$Q = Q_0 \cos{(2\pi\nu_{vib}t)}. \tag{3}$$

Here Q_0 is the amplitude of displacement for the vibration, and ν_{vib} is the frequency of the molecular vibration which can be obtained from the vibrational energy E_{vib}:

$$E_{vib} = (\nu + \frac{1}{2})h\nu_{vib} \tag{4}$$

where ν is the vibrational quantum number and h being the Planck constant. The polarizability can, assuming the displacement is small relative to bond length, be expanded using a Taylor expansion to obtain the first order term as:

$$\alpha = \alpha_0 + \frac{\partial\alpha}{\partial Q}Q \tag{5}$$

next, inserting this into eq.2 and replacing Q with eq.3 yields:

$$\begin{aligned} P =& \alpha_0 E_0 \cos{(2\pi\nu_0 t)} + \frac{\partial\alpha}{\partial Q}Q_0 E_0 \cos{(2\pi\nu_{vib}t)}\cos{(2\pi\nu_0 t)} & (6) \\ =& \alpha_0 E_0 \cos{(2\pi\nu_0 t)} + \left(\frac{\partial\alpha}{\partial Q}\frac{Q_0 E_0}{2}\right)\left[\cos{(2\pi(\nu_0 - \nu_{vib})t)} + \cos{(2\pi(\nu_0 + \nu_{vib})t)}\right] & (7) \end{aligned}$$

resulting in three terms, each with one frequency. The Rayleigh term contains unshifted ν_0 while the Stokes and anti-Stokes terms have frequencies $\nu_0 - \nu_{vib}$ and $\nu_0 + \nu_{vib}$ respectively. An important observation is that both Raman terms require that $\frac{\partial\alpha}{\partial Q} \neq 0$ to be active, which explains the requirement on polarizability variation for Raman activity. As shown, the classical description does supply a mathematical description of Rayleigh scattering, Raman scattering and the behavior of the induced dipole moment. In the case of a solid, Raman scattering is not limited to discrete vibrational levels and the lattice vibrations are distributed in acoustic bands within the electronic band structure [34].

In Raman spectroscopy the emitted light is then a spectrum containing information on the different vibrational and rotational energy levels of a system. More specifically, the spectrum is centered around the Rayleigh peak which has the same photon energy or wavelength as the incoming radiation with Stokes peaks (red shifted) on one side and anti-Stokes peaks (blue shifted) on the other [34]. The Stokes and anti-Stokes spectra contain the same spectral peaks and are mirrored around the Rayleigh peak in terms of peak shift; however, the relative intensities of the anti-Stokes and Stokes spectra depend on the distribution of electrons in the energy structure, and anti-Stokes scattering generally has lower intensity as it requires electrons in excited initial states. The intensity of the Raman scattering depends on the Raman cross-section which in turn relates to the optical properties and energy structure of the sample. For solid samples such as carbonaceous materials, the band structure must be considered [34].

The polarization dependence of Raman scattering is well known and is used in different applications [23, 34]. The fundamental principle behind the polarization dependence originates from the anisotropic polarizability of the scatterer. Electrons in a system that are subjected to external oscillating fields will be displaced and the magnitude of the displacement depends on the bond strength of the electron-nuclei interaction. As stated earlier the relative motion of the nuclei must result in a changing polarizability throughout the motion, for a transition to be Raman active. However, for certain systems the polarizability is not isotropic. Linear homonuclear molecules and crystalline solids are scatterers with polarization dependence as the polarizability of these materials depends on the equilibrium position of the nuclei. For a linear homonuclear molecule, a stretching vibrational mode produces a non-zero change in polarizability along the inter-nuclear axis. However, perpendicular to the inter-nuclear axis the polarizability change is small in comparison [34]. If then a linearly polarized source is used to excite a group of molecules, those with inter-nuclear axis parallel to the incident light will Raman scatter orders of magnitude more than molecules with inter-nuclear axis perpendicular to the light polarization. In a solid the crystalline structure determines the anisotropic polarization. As a result, with carbonaceous materials the degree of crystallization (in other words graphitization) affects the polarization sensitivity of Raman scattering in the sample. For the purpose of experiment, it is common to use two polarizabilities α for the sample, one perpendicular to incident light and one parallel. By measuring Raman intensities with two polarizers in perpendicular and parallel alignment the depolarization ratio can be determined as the intensity ratio $I_{perpendicular}/I_{parallel}$, where perpendicular and parallel is relative to the polarization of the incoming light [34].

2.3.2 Raman spectra of carbonaceous materials

The Raman spectra of a few different carbonaceous materials can be seen in fig.4 [36, 37] that are sorted by structural order from top to bottom. The spectra range from 500 to 4000 cm^{-1}, which includes the first order (800-1700 cm^{-1}) and second order (2300-3500 cm^{-1}) Raman peaks of graphene, graphite, ethylene flame soot and two types of amorphous carbon. Raman spectra of carbonaceous materials are generally superimposed on a fluorescence background which originates from organic compounds [38]. The peaks in the spectra correspond to lattice vibrations of different chemical compounds and bond types. The full-width at half-maximum (FWHM) of the peaks is related to the structural order of these, as is the relative intensities which relate to both structural properties and morphology [25].

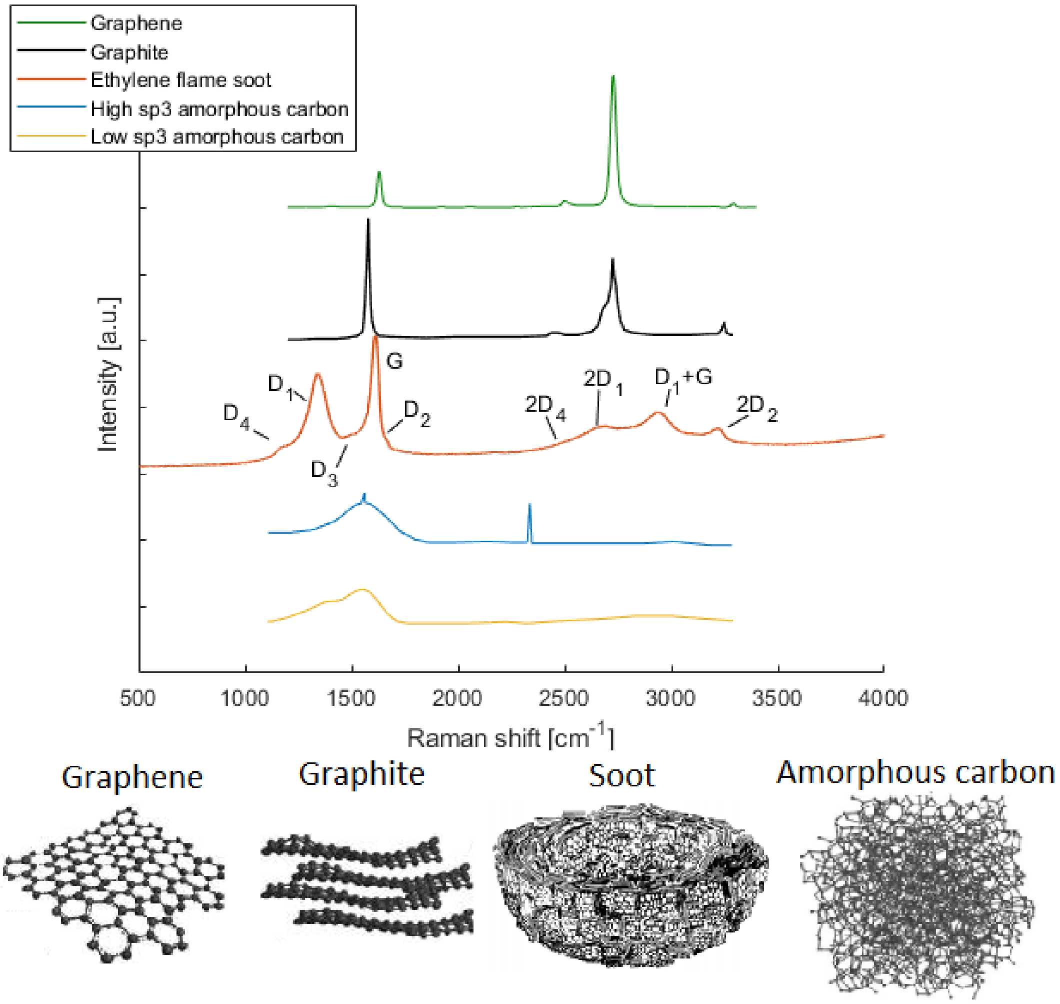

Figure 4: *Raman spectra of different carbonaceous materials with a decreasing structural order from top to bottom, as well as illustrations of the different forms of carbon material. The green line shows the spectrum of graphene, the black line shows the Raman spectrum of highly ordered graphite, the red line shows the spectrum obtained from soot from an ethylene flame while the blue and yellow lines show two different types of amorphous carbon with high and low sp*^{3} *content respectively. The ethylene flame spectrum is also marked with the peaks that build up the Raman spectrum. The data plotted was obtained from refs. [36, 37] while illustrations of materials were obtained from [12, 39, 40].*

The observed spectra in fig.4 are produced with visible excitation wavelengths. These peaks are defined in literature regarding Raman spectroscopy in sp^2 dominated samples and are detailed in table 1 along with the suggested corresponding lattice vibration symmetry [25, 26, 41]. The spectrum can be separated into two ranges, the first (800-1700 cm^{-1}) and second order (2300-3500 cm^{-1}) spectra. The peaks that have been primarily studied are the D$_1$ and G peaks in the first order where the G peak originates from sp^2

bond stretching in aromatic rings. Other sp^2 bound structures such as olefinic chains will also contribute. The D_1 peak is one of the disorder induced peaks, resulting from aromatic ring breathing modes, which are Raman inactive in perfect graphitic lattices [38]. In disordered materials however, doubly resonant Raman processes can occur, activating the breathing modes [42]. Other first order peaks include D_2 which corresponds to graphitic surface vibrations, D_3 resulting from amorphous sp^2 and sp^3 [25] phase and D_4 which is proposed to originate from sp^2 and sp^3 bonds in polyene-like structures [25]. The D_5 peak has been observed in some samples and is suggested to originate from trans-polyacetalene segments on edges of polyaromatic clusters, however due to its irregular appearance it is not well understood [26].

The second order spectrum contains peaks which represent two-phonon processes, in other words combination peaks or overtones of the first order and are related to doubly resonant processes. In fig.4 the $2D_1$ peak is active for graphite, however the D_1 peak is not present. The general explanation for this is that two-phonon processes [43], where two phonons are produced in the Raman scattering, preserve momentum by back-to-back scattering phonons, allowing $2D_1$ to be active even in graphite. Peaks have also been observed in the range between the first and second order and are often attributed to sp bonds in polycumulene and polyyne [44].

The general method of obtaining these peak parameters is to fit or deconvolute the spectrum using Lorentzian or Gaussian peak shapes with a photoluminescence background. However, there is not one specific protocol that has been established as different protocols have been shown to be appropriate for different samples. The protocols diverge in terms of the number of peaks which are fitted and the shape of the peaks. For amorphous samples it is common to only fit two peaks, D and G, with Gaussians and in these cases the peaks are often referred to as bands, as disorder broadens the peaks to a point where smaller peaks are indistinguishable. For ordered samples it has been noticed that the G peak has varying degrees of symmetry, leading to protocols using Breit-Wigner-Fano (BWF) functions to fit the G peak [45]. It is important to note that a BWF-function has a peak position that is different from ω_G (corresponding to the peak position of a Lorentzian) due to the asymmetry and is instead positioned at $\omega_{max} = \omega_G + \frac{HWHM_G}{2q}$ where q is the asymmetry factor and must be negative [46]. The theoretical motivation for why it is appropriate to use a BWF-function comes from the phonon band structure in carbon. That is, the phonon density of states for the G peak describes a line transition coupled to a continuum. This reasoning is however obtained from graphene phonon density of state and applying it to other carbon materials is an approximation [43, 45]. For cases

Table 1: *Primary Raman peaks of soot*

Peak designation	Raman shift [cm^{-1}]	Type of vibration
G [25]	~1600	C-C sp^2 bond stretching, E$_{2g}$ symmetry
D$_1$ [25]	~1350	Breathing mode of aromatic rings, A$_{1g}$ symmetry, doubly resonant
D$_2$ [25]	~1620	Surface vibrations of graphitic crystals, E$_{2g}$ symmetry, doubly resonant
D$_3$ [25]	~1470	Amorphous sp^2 vibrations local defects
D$_4$ [25]	~1200	sp^2 and sp^3 bond stretching, A$_{1g}$ symmetry
D$_5$ [26]	~1170	sp^2 stretching and C-H oscillation, from trans-polyacetylene structures
G+D$_1$ [26]	~2950	Combination peak, resonant G and D$_1$
2D$_1$ [26]	~2740	Overtone of D$_1$, two-phonon
2D$_2$ [26]	~3200	Overtone of D$_2$,
2D$_4$ [26]	~2500	Overtone of D$_4$,

where D$_2$ is fitted there are uncertainties caused by the close proximity of G and D$_2$, as overlap can cause inconsistent results from deconvolution. As D$_2$ originates from ordered graphitic surface layers, it is often assumed to be stationary at around 1620 cm^{-1} which can give consistent results [25].

2.3.3 Determining properties of carbonaceous materials from Raman spectroscopy

Aside from chemical group and order degree information detailed in the previous section, Raman spectroscopy can be used to extract structural and optical information of carbonaceous materials. Indeed, correlations have been found between the ratio I_D/I_G and the in-plane length of polyaromatic clusters, as measured by TEM or X-ray diffraction, which is possibly due to the origin of the peaks [43, 47]. As the G peak results from sp^2 bond stretching in aromatics and olefinic chains while the D peak is a result of disorder, the ratio between them relates to disorder relative to sp^2 content. L_a is defined as the in-plane length of polyaromatic units which also relates to disorder in sp^2 structures. From this, there have been several attempts to find a relation between I_D/I_G and L_a. A prominent relation that has been discussed is the Tuinstra-Koening relation [47], stating that:

$$\frac{I_D}{I_G} = \frac{44}{L_a[\text{Å}]} \tag{8}$$

where the coefficient 44 is specifically determined for excitation at 514 nm and is expected to change with excitation wavelength due to the dispersive behavior of D [45]. However, as the G peak intensity also depends on the olefinic contents, for samples that contain a high fraction of olefinic chains the value of L_a will be overestimated when using eq.8. The relation was tested for several samples and it was observed that the correlation was not consistent for different values of L_a [38] and eq.8 not accurate for L_a bellow 2 nm. For $L_a < 2$ nm, the relation instead behaved as [38]:

$$\frac{I_D}{I_G} = 0.0055(L_a[\text{Å}])^2. \tag{9}$$

The cause of the different relations has been suggested to arise from the D peak activation restrictions [38]. For L_a smaller than 2 nm, the probability of finding ordered polyaromatic rings in a carbon cluster is small and the D peak intensity is proportional to the area of the cluster. If L_a is larger than 2 nm, the increase in size becomes a restriction on I_D as the aromatic ring must be at the edge of a cluster to be Raman active while the relation becomes similar to the ratio between circumference and area, meaning inverse relation to L_a. There are limitations on using this formulation as well, including the presence of olefinic chains [38].

Equations 8 and 9 are both determined for 514 nm excitation and in literature modified versions have been constructed to account for wavelength dependence. The following relations have been suggested in [45] and eq.10 is analogous to the Tuinstra-Koening relation:

$$I_D/I_G = \frac{44}{L_a[\text{Å}]} \cdot \left(\frac{2.41}{E_L[\text{eV}]}\right)^4 \tag{10}$$

In eq.10 the additional factor comes from the expected wavelength dependence of the D_1 peak intensity, which is reportedly proportional to E_L^{-4} for graphene [48]. The value 2.41 eV corresponds to 514 nm and E_L is the excitation wavelength used in the measurement. Using eq.10 with eq.9 and applying continuity at 20 Å allows correction of the relation from ref. [38], giving:

$$\frac{I_D}{I_G} = 0.0063(L_a[\text{Å}])^2 \tag{11}$$

for 532 nm excitation.

The I_D/I_G ratio is not the only suggested way to determine L_a, other methods including using the FWHM of the G peak and peak positions were also considered [45]. These have all been suggested as possible index of graphitization, which can be used to give a relative value for structural order in the material for comparing different samples.

$$\Gamma_G = 71 - 5.2 \cdot L_a. \tag{12}$$

For eq.12 the half-width at half-maximum (HWHM) of the G peak is instead used where the peak is fitted using a BWF function. The relation was suggested in [45], as the Tuinstra-Koening relation has been shown to give inconsistent results for different types of carbonaceous materials such as pyrocarbons [48, 49]. The definition of the intensity is also not well defined, as some papers treat the integrated intensity of the peak whereas others use peak intensity. These inconsistencies have resulted in attempts to find alternatives, including eq.12. It should be noted that eq.12 is for L_a between 2 and 10 nm [45].

As the optical band gap of individual PAHs depends on the amount of aromatic rings in the PAH, it has been suggested that the band gap of soot and similar materials should be related to L_a. As the polyaromatic unit length is dependent on the number of rings and the π state band gap of PAH molecules is related to the medium-range lattice interactions, a relation between L_a and band gap has been motivated [38, 50]. This would provide a useful tool in characterizing the optical properties of soot using Raman spectroscopy, however there are currently only estimations from measurements of the band gap using, for example, excitation measurements and comparing to L_a as calculated from Raman spectra. Estimations based on using the slope of the fluorescence background compared to the G peak intensity have been tested for amorphous carbons as well. However, these are motivated for samples with optical band gaps larger than the excitation energy, allowing sub band gap PAH clusters to be probed by photoluminescence [38].

3 Method

3.1 Samples

Carbon black samples can be seen in table.2 and were contributed by Norcarb Engineered Carbons AB with characteristic properties used in carbon black industry.
The values of Statistical Thickness Surface Area (STSA) and Iodine number were specified by the manufacturer along with the samples and are determined from techniques that are used for describing classes of carbon black in terms of surface area for soot agglomerate particles. STSA is determined by surface adsorption of nitrogen while Iodine number is similar, instead using iodine adsorption. CXN-550, ECX-S206 and PXalpha-A samples were given in two forms, pressed and unpressed, where the pressed samples had been com-

Table 2: *Characteristic data for carbon black samples from Norcarb Engineered Carbons AB*

Designation	STSA [m^2/g]	Iodine number [mg/g]
INR-A	—	41.5
INR-B	—	90.8
INR-C	—	125.8
CXN-550	39	43
ECX-S206	19	19
PXalpha-A	85	118

pressed after manufacturing. The INR samples were standardized carbon blacks which have been heat treated, however the STSA values for these samples were unavailable.

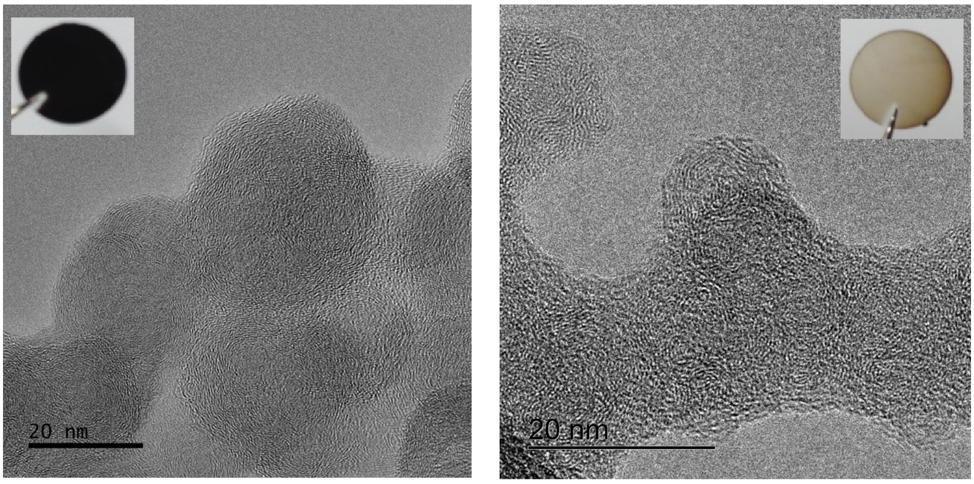

OP1 OP6

Figure 5: *HRTEM images of OP1 and OP6 soot [14] with images of soot samples on sapphire windows to show sample color. From the HRTEM images the structural disorder can be observed as the orientation of graphitic layers in the outer regions of the soot particles where the layers appear more parallel in OP1 soot.*

Raman spectra of soot produced by a MiniCAST (Miniature Combustion Aerosol Standard) 5201C soot generator (mini-CAST Jing Ltd. [15]) was used for comparison with the carbon black samples. In the MiniCAST generator, soot is produced using a propane-air co-flow diffusion flame where a stream of nitrogen across the top of the flame quenches flame chemistry and sweeps soot aerosols into a flow of dilution air. Different factory default operation points (OP) are defined with varying flows of dilution nitrogen (different from extinguishing nitrogen), air and fuel. Soot generated at different operation points has differences in the produced amount per time unit, size and properties [14, 15]. The operation points that are used for this thesis are OP1 and OP6 which can be described as being similar to mature and immature soot, respectively [15]. Soot samples were collected by inserting sapphire windows into the exhaust of the miniCAST soot generator.

In figure 5 HRTEM images of the two miniCAST soot types can be observed, showing a higher degree of structural order in the OP1 soot as displayed by the ordering of layers in the shell of the particles. The color of the samples also differs, and OP6 has a brown and yellow color which is expected for immature soot while OP1 soot is black, similar to mature soot [24].

3.2 Raman setup

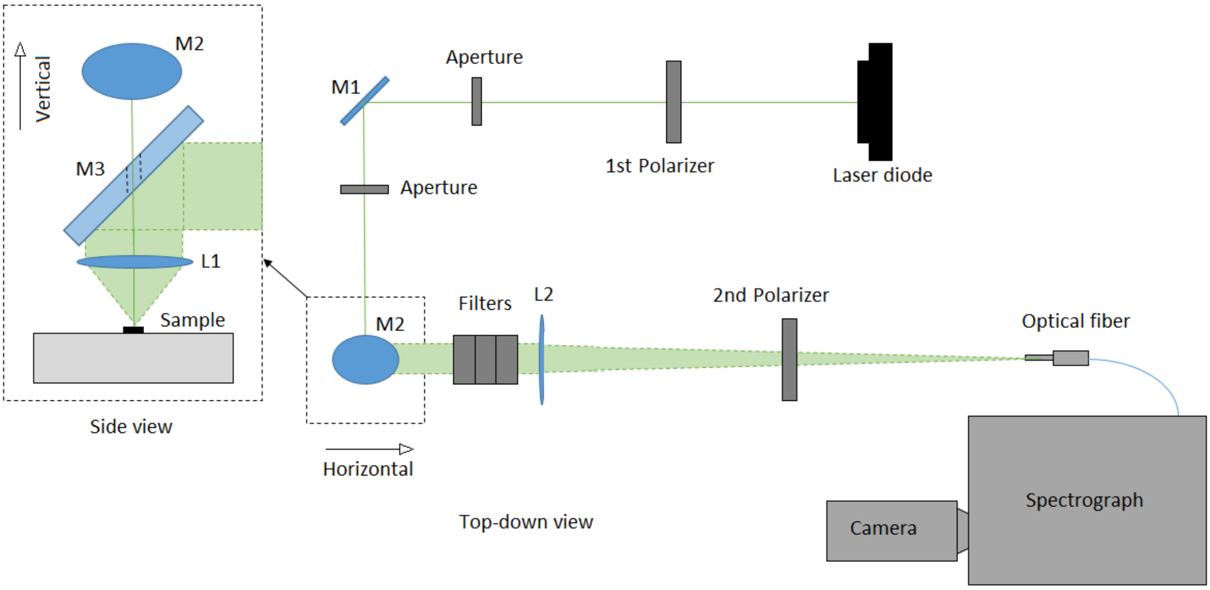

Figure 6: *Schematic of the Raman setup used for the experiment. Here M1, M2 and M3 represent mirrors while L1 and L2 are focusing lenses with focal lengths of 30 mm and 150 mm respectively. For measurements in controlled environment and heating, the Linkam heating stage is placed at the sample holder with the sample inside.*

Raman spectra of the samples were measured using our home-built Raman spectroscopy setup. The schematic of the setup can be seen in fig.6 where an unpolarized 532 nm diode laser (Thorlabs, DJ532-40) source was used. A maximum power density of approximately 6 mW/mm^2 was used for this experiment. Using mirrors and apertures the beam was directed through a drilled hole in a 50.8 mm broadband mirror and then focused on the sample by a 30 mm focal length lens. The back scattered light was collected using the focusing lens and reflected on the broadband mirror towards a series of filters to remove Rayleigh scattering and anti-Stokes signals. These filters consist of a long-pass filter (Thorlabs, FEL0550) with a cut-on wavelength of 550 nm, a short-pass filter (Thorlabs, FES0650) with a cut-off wavelength of 650 nm, as well as a notch filter (Thorlabs, NF533-17) with a central wavelength of 533 nm and FWHM of 17 nm to further attenuate the Rayleigh scattered light. Using a lens with a focal length of 150 mm the signal was focused on an optical fiber coupled to a IsoPlane SCT320 spectrograph

(Princeton Instruments). The signals were then recorded by a CCD camera (Andor technologies, Newton DU94ON-BV) with 2048 by 512 pixels.

The spectral resolution for the setup has been calculated to be less than 14 cm^{-1}. Three gratings were used for acquisition of spectra; one narrow band grating (600 l/mm) to acquire the first and second order Raman bands separately with higher dispersion, one broad band (150 l/mm) to acquire both bands simultaneously as well as an intermediate grating (300 l/mm) that allowed acquisition of first and second order simultaneously with higher resolution compared to the 150 l/mm grating. The setup was constructed to facilitate heat treatment using a LINKAM (TLI1200) heating stage with controls for heating rate, maximum temperature and time during which a specific temperature is maintained [51].

For polarization measurements, two linear polarizers were used, the first placed after the laser source to polarize the laser radiation and the second placed between the fiber coupling lens and the fiber. The second polarizer was used as analyzer and was rotated for a range between parallel and perpendicular polarization relative to the incoming polarization. Spectra were recorded for two carbon black samples, CXN-550 and INR-A, as they have different characteristics in terms of cluster size and structural order which is expected to lead to a difference in peak depolarization.

In the study of the influence of excitation power and exposure time on Raman signals of soot, a polarizing beam splitter was used. This beam splitter was inserted in front of the laser, with transmission direction towards the Raman setup and the reflected beam directed onto a power meter (Thorlabs, PM400K).

Laser effects on the miniCAST soot samples were studied with variations of power and exposure time on the sample. For the power dependence of the Raman and fluorescence signals, neutral density filters whose optical density varied from 0.1 to 1 were used to reduce the laser intensity instead of varying the driving current to avoid mode jumps in the diode laser. The samples were kept in a nitrogen gas atmosphere to avoid oxidation. The effect of laser exposure as a function of time was tested in both air and nitrogen atmosphere, and was performed by irradiating the sample continuously while recording spectra for five minutes followed by five minutes until the next measurement starts.

Heating effects on soot were studied using the Linkam heating stage in air. This was performed for the purpose of studying the possible restructuring of soot under heating when influenced by oxidation, as well as variations in fluorescence background. This was done for a temperature range from 25 °C up to the temperature at which the soot was completely evaporated or oxidized and Raman spectra disappeared. This process depends on experimental atmosphere and soot type. The sample was kept under a constant flow of gas during the measurement series to remove evaporated material as this would otherwise be deposited on the window in the lid of the heating stage and affect the measurement. The flow was kept low to avoid disturbance of the sample. After heating the Linkam system, temperature was reset to room temperature where all spectra were acquired, to avoid spectral changes during acquisition. Additionally, thermal radiation emitted by the ceramic heating element in the Linkam heating stage at temperatures above 500 °C could be avoided this way. This would influence the spectrum and could possibly saturate the camera as the acquisition settings were optimized for Raman intensities, several orders of magnitude lower.

3.3 Deconvolution protocols

As stated in section 2.3.2, deconvolution is used to obtain the spectral peak parameters and several protocols are used for the first order spectra. A common method of choosing protocol is to choose the protocol that gives the highest Goodness of Fit (GoF), specifically an adjusted R-square closest to 1 and low Normalized Root Mean Square Error (NRMSE)[43, 45]. The choice of protocols followed different suggestions in literature and the protocol used utilized a BWF function for the G peak and three Lorentzian peaks for D_1, D_4 and D_5, however for most literature examples D_5 is not fitted as it is not observed. It is common to observe a shoulder on the D_1 peak as a result of D_4. Methods including or excluding D_2 were tested due to the uncertainty introduced by close proximity of G and D_2. An additional peak was fitted at 826 cm^{-1}, as a peak was observed here for the carbon black samples. Figure 7 shows an example of a deconvolution protocol.

The second order spectra were deconvoluted according to the protocol from ref. [25], where four peaks were fitted as Lorentzian functions, corresponding to $2\mathrm{D}_4$, $2\mathrm{D}_1$, D_1+G and $2\mathrm{D}_2$ for spectra where the fitting protocol could separate the peaks. For samples where the second order peaks were indistinguishable, generally a single Gaussian peak was fitted for the entire second order spectrum by the fitting protocol.

As the nitrogen peak is observed, an oxygen peak will also be present at 1556 cm^{-1}, however it is weaker than the nitrogen line and the influence on the spectra is negligible in relation to the G peak which can be seen in fig.8.

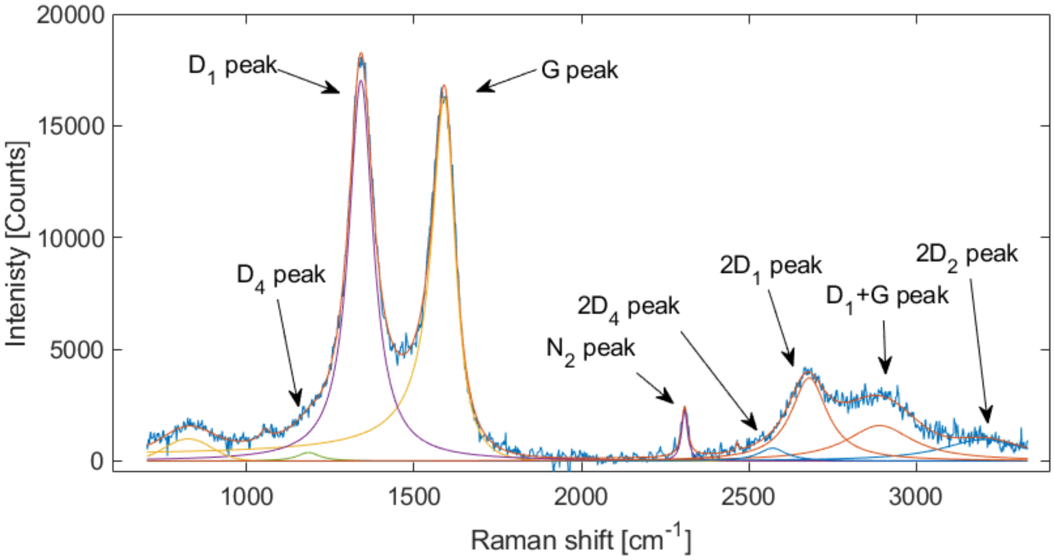

Figure 7: *Example of a deconvolution, including the individual fitted peaks, obtained Raman spectrum (blue, after fluorescence subtraction) and the total fitted spectrum (red). The fluorescence background is fitted simultaneously as the spectrum and is subsequently subtracted. The peaks seen here are* D_4 *(* $\sim$*1180 cm*$^{-1}$*),* D_1 *(* $\sim$*1350 cm*$^{-1}$*), G (* $\sim$*1590 cm*$^{-1}$*),* $2D_4$ *(* $\sim$*2570 cm*$^{-1}$*),* $2D_1$ *(* $\sim$*2680 cm*$^{-1}$*),* D_1*+G (* $\sim$*2890 cm*$^{-1}$*) and* $2D_2$ *at (*$\sim$*3210 cm*$^{-1}$*). The* N_2 *peak that is observed at* $\sim$ *2330 cm*$^{-1}$ *is due to nitrogen in the laser path and is not a property of the carbon black.*

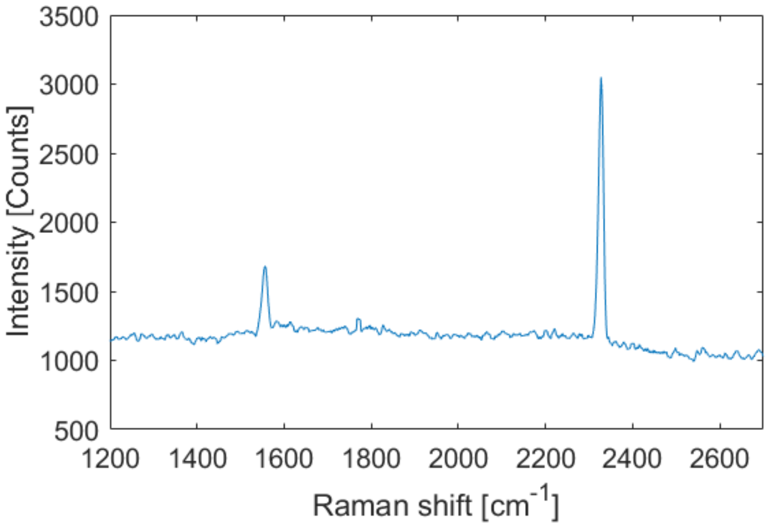

Figure 8: *The spectral contribution of* O_2 *and* N_2 *Raman peaks. The* O_2 *peak at 1556 cm*$^{-1}$ *is significantly smaller than the* N_2 *peak at 2327 cm*$^{-1}$*, and will be negligible in comparison to the G peak.*

4 Results and Discussion

In this section, the results from the experiments will be presented, starting with the structural information that was obtained for the different soot and carbon black samples. This is then followed by the influence of the laser on the samples in terms of power and exposure time, and finally a section discussing the uncertainties of the fitting protocol.

4.1 Structural study of carbon black and miniCAST soot

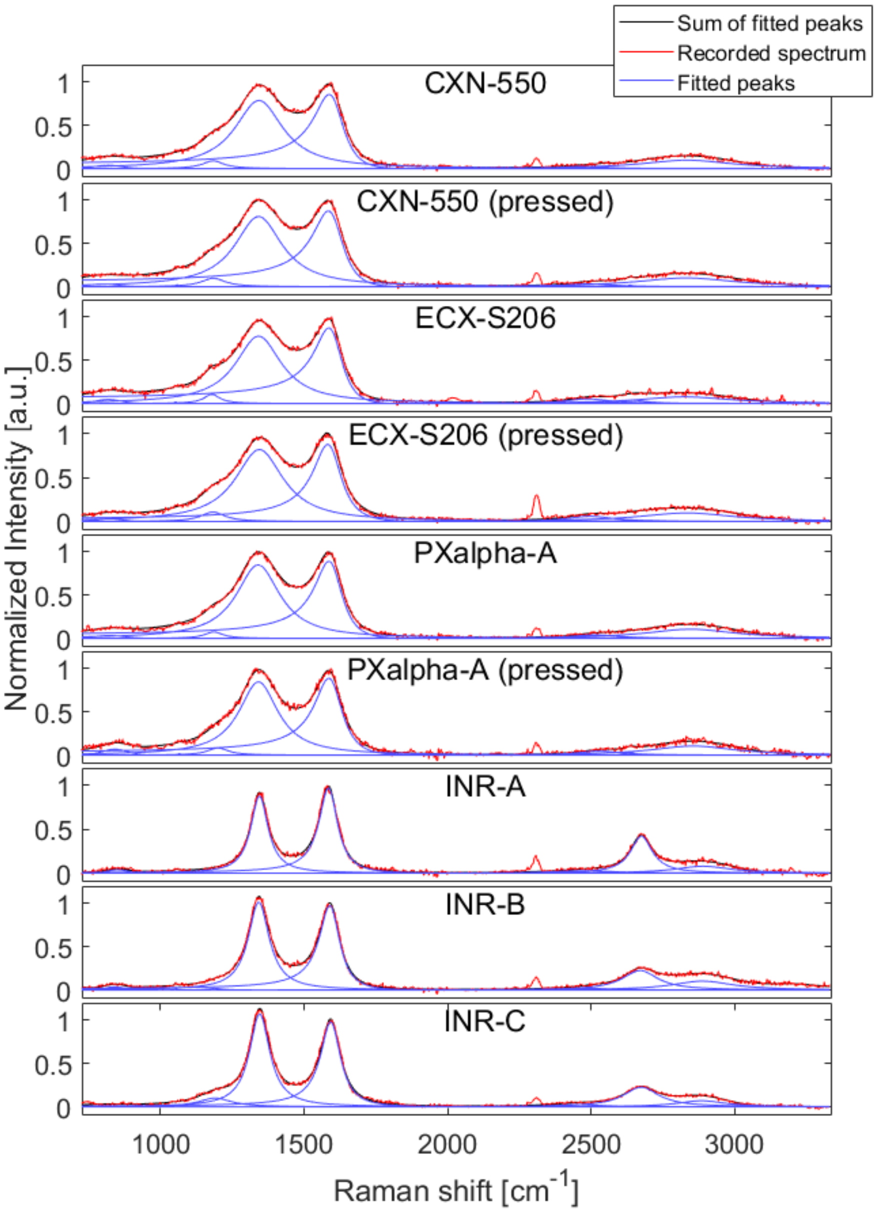

Figure 9: *Recorded Raman spectra of carbon black samples with fluorescence background subtracted, including the total fitted spectra and individual peaks. The fitting method used for these spectra uses a BWF-function for the G peak, Lorentzian functions for D_1, D_4, D_5, $2D_1$, $2D_2$, $2D_4$ and Gaussian functions for D_1+G and ~830 cm^{-1} peaks. The N_2 peak at approximately 2300 cm^{-1} is fitted as well to account for its spectral contribution but not included in the plotting of the fitted spectra. The NRMSE and adjusted R-square of different model for each spectrum are shown in tab.4*

Figure 9 gives an overview of the carbon black spectra with spectral deconvolution. From the spectra it can be seen that the heat treated samples (INR) are distinct from the other carbon blacks in terms of FWHM of the G and D_1 peaks and relative intensity of the $2D_1$ peak as heating amorphous carbon is expected to increase graphitization and polyaromatic unit length. The reduction in polyaromatic mean size should then be reflected in the relative intensities of the D_1 and G peaks as described in section 2.3.3 and for samples with polyaromatic mean size larger than 2 nm the intensity of the D_1 peak should increase relative to the G peak, however for samples with polyaromatic mean size of less than 2 nm the intensity of D_1 is reduced. The FWHM of the G peak decreases from around 125 to 80 cm^{-1} from the CXN-550 sample to the INR-A sample, indicating that the polyaromatic unit-length could increase above 2 nm as $FWHM_G$ decreases bellow 100 cm^{-1} [43, 45]. To determine the best method for estimating polyaromatic unit length, L_a was calculated from the $FWHM_G$ using eq.12 and the peak intensity ratio of G and D_1 using eqs.11 and 10, which produces similar results only for the carbon black samples. The resulting values of L_a can be seen in fig.10, plotted against the $FWHM_{D_1}$ as this is described as a good measure of structural order [43]. The fluorescence background is subtracted before determination of the peak intensities in this study, and it should be noted that the values of the intensity ratio would be different if this was not performed.

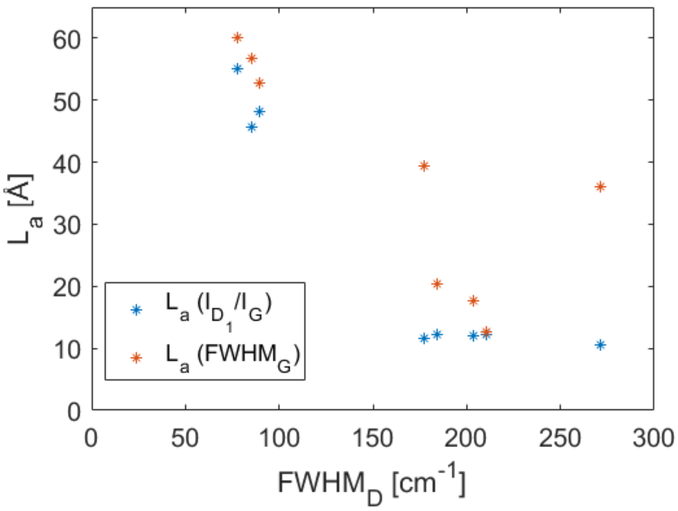

Figure 10: *L_a estimated using two methods, $FWHM_G$ in accordance with [45] and using the intensity ratio between D_1 and G [38], plotted against $FWHM_D$, as it has been shown to be a possible measure of maturity for carbon black [43]. The two deviating points for the $FWHM_G$ method are the miniCAST samples and their deviation is likely due to having L_a of less than 2 nm, meaning this method is not suitable for these samples.*

The values of L_a are estimations and to control these values there are a few techniques that could be used for comparison such as high resolution TEM and X-Ray diffraction. Previously, miniCAST samples have been investigated with high resolution transmission electron microscopy (HRTEM) [14]. In these measurements the geometric mean fringe length of OP6 was found to be ~ 5.4 Å, approximately half of L_a estimated from this measurement. The relations in eqs.10 and 11 are constructed from specific samples and should be cautiously used, as there is no relation that is observed to be accurate universally. The estimation of L_a is dependent on sample due to the large amounts of variables that can affect the peak shapes [43], as well as the deconvolution protocol.

The Raman spectra of the pressed carbon black samples were measured and compared to the powder counterparts. The resulting difference between pressed and non-pressed sample spectra were within the noise threshold and as such it would seem that the pressing procedure does not affect the nano-scale structures. The difference between the deconvoluted spectra of pressed and non-pressed samples were also within the error of the fitting protocol.

Figures 11a and 11b show the different Raman spectra of the miniCAST samples. The main differences are the strong fluorescence contribution from OP6 and the peak intensity ratio of the fitted peak between D_1 and G is different, ~ 0.85 for OP1 and ~ 0.71 for OP6. OP6 also contains a shoulder peak (D_1') peak at 1250 cm^{-1} with higher intensity relative to G than OP1. Notably, the Raman intensity for OP1 is less than that of OP6. OP1 and the non-INR carbon blacks have a strong resemblance in terms of distinguishable peaks, FWHM and fluorescence background while OP6 shows broader peaks, one single broad second order peak and a large fluorescence contribution. The spectra then describe a trajectory of structural order from OP6 as disordered soot relative to the other samples, followed by OP1 and the majority of the carbon blacks. These being soot types that have been seen to behave similar to more ordered soot (OP1) and less structurally ordered soot (OP6) [14, 15]. The INR samples can then be described as having a high degree of structural order relative to the other carbon blacks, as the INR samples have been annealed post-flame. During heating in inert atmosphere, elements other than carbon (hydrogen and oxygen primarily) are reduced and clustering is increased by the increase in sp^2 bonds relative to sp and sp^3.

The OP6 spectrum shows a shoulder on the D_1 peak at 1250 cm^{-1}, which corresponds to sp^2 and sp^3 structures according to [41]. In the OP6 spectrum a broad weak peak at 2133 cm^{-1} is also present. This peak is a result of sp bonds in cumulenic and polyynic structures [26]. Due to the broadening of the second order peaks, individual peaks become indistinguishable for all samples except the INR samples, resulting in one band that was not possible to deconvolute. For the INR samples however, the intensity of the $2D_1$ peak increases in relation to the G peak as the FWHM of the peaks decrease. The $2D_1$ peak is

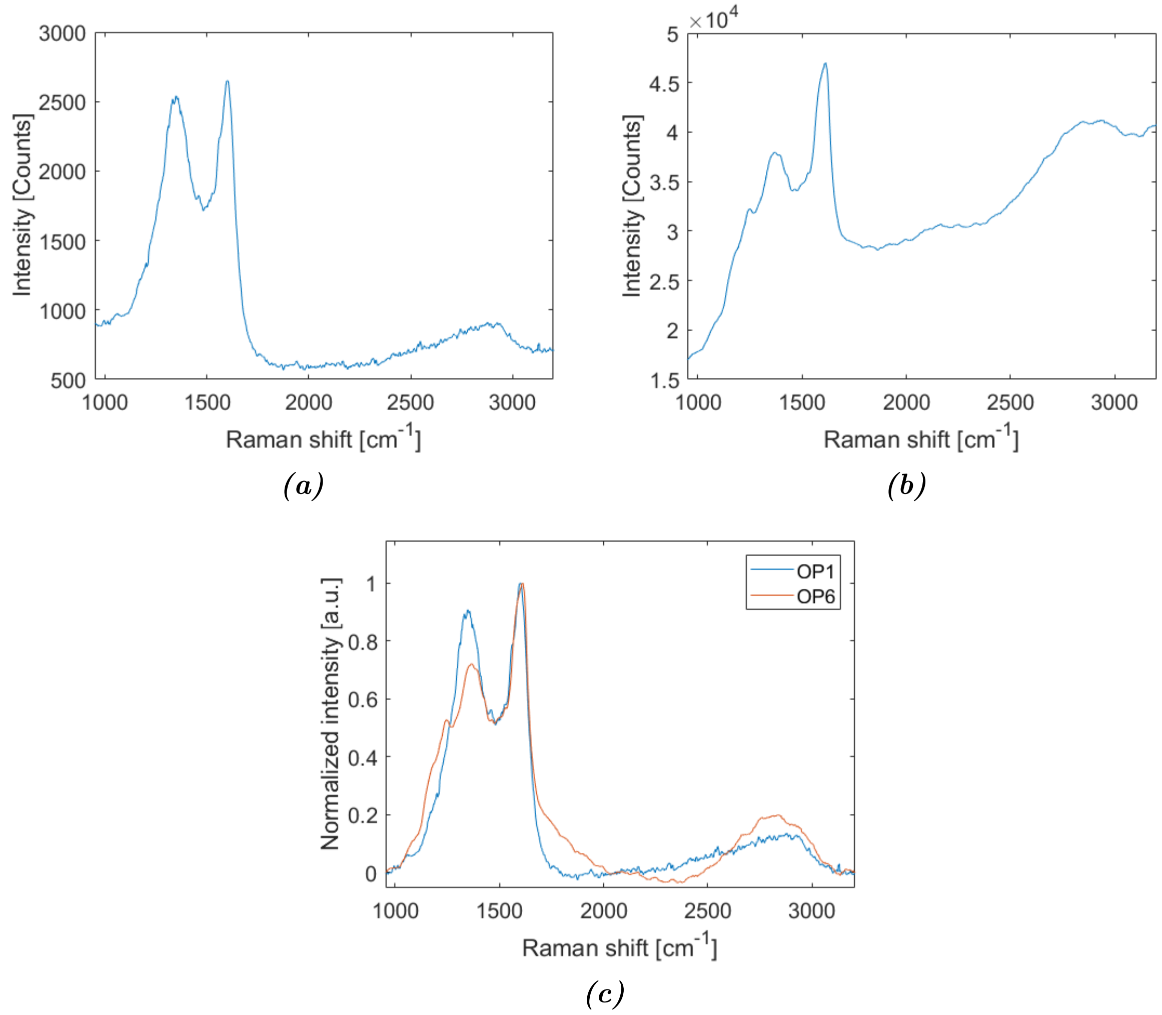

Figure 11: *Raman spectra of OP1 soot (a) and OP6 soot (b) before fluorescence subtraction and both spectra normalized after fluorescence subtraction (c).*

expected to be present in ordered materials such as graphene due to the two-phonon processes preserving momentum while other second order peaks decrease as order increases [36, 43].

In table 3 the different peak widths of D_1 and G can be seen along with I_{D_1}/I_G. The table shows that the OP6 soot has the broadest peaks, followed by the carbon black samples and OP1 except the heat treated samples (INR), which have the narrowest peaks. Increasing maturity is expected to reduce the peak width as the material obtains a larger fraction of ordered structures. As the material becomes increasingly graphitic, the phonon transitions are decreasingly perturbed by lattice inhomogeneities, resulting in narrowing of the peaks [36, 45].

Using the relative peak intensity of D_1 and G, the polyaromatic unit length can be estimated as described in eqs.10 and 11 or alternatively eq.12 which are both shown in fig.10. As expected, eq.12 does not seem suitable for the miniCAST samples, as the estimated

Table 3: *FWHM of* D_1 *and G, as well as* I_{D_1}/I_G *and estimated* L_a *from eqs.10 and 11 for different samples types.*

Sample	FWHM$_{D_1}$ [cm^{-1}]	FWHM$_G$ [cm^{-1}]	I_{D_1}/I_G	L_a (I_{D_1}/I_G) [Å]	L_a (FWHM$_G$) [Å]
INR-A	77.9	79.6	0.91	55.1	60.0
INR-B	89.6	87.1	1.04	48.2	52.8
INR-C	85.1	83.0	1.1	45.7	56.7
CXN-550	210.8	128.8	0.93	12.2	12.7
ECX-S206	203.5	123.7	0.92	12.05	17.6
PXalpha-A	184.5	120.7	0.95	12.3	20.48
OP1	177.3	101.1	0.85	11.6	39.3
OP6	271.1	104.6	0.71	10.6	36.0

polyaromatic unit length describes a mature soot. Out of the methods used here, the protocol that follows expectations with regards to maturity is using the Tuinstra-Koening relation [45] for carbonaceous materials with a FWHM$_D$ smaller than 100 cm^{-1} while samples with broader D$_1$ peaks follow the relation described by Ferrari and Robertson [38]. These results can be seen in fig.10.

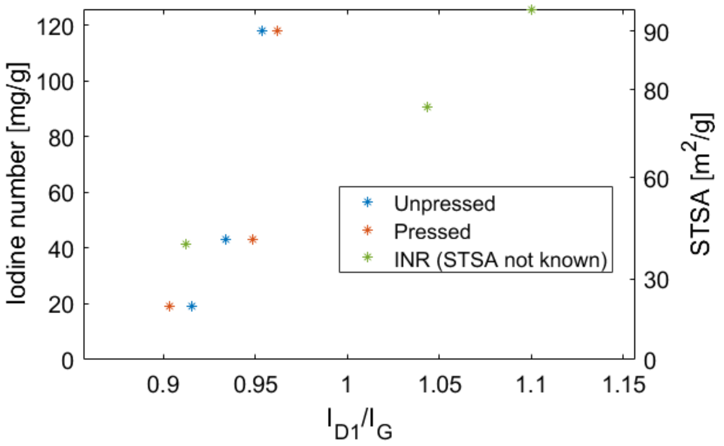

Figure 12: *Correlation between Iodine number and* I_{D_1}/I_G *in Raman spectra for three types of carbon black. The INR samples do not follow the same trend as the other carbon black samples, yet a common trend can be described as an increase in surface are estimation values follows an increase in the peak intensity ratio.*

Figure 12 shows the iodine number, STSA and I$_{D_1}$/I$_G$ for the carbon black samples. It should be noted that STSA is not specifically known for the INR samples. A possible trend can be seen, as the increase in the I$_{D_1}$/I$_G$ ratio also corresponds to an increase in the measures of surface area. As I$_{D_1}$/I$_G$ is related to the disorder content, this could be reflected in terms of properties such as porosity. If then the surface is structurally dependent on the disorder, it would be possible that the surface adsorption is similarly affected by the relative contents of sp^2 and amorphous carbon. The amount of data points is however limited, and for more certain results a larger amount of samples would be necessary.

4.2 Effects of laser interaction and environment

In this section the results containing laser exposure time, power dependence, polarization and heating are presented. The samples used for all these measurements were OP1 and OP6 except the polarization measurements which were performed on carbon black samples INR-A and CXN-550. The purpose of this was to compare the different effects on a structurally ordered soot and a less ordered soot. For the power dependence it is expected that the Raman signal strength is linearly related to the laser power, as the dipole moment is linearly proportional to the electric field strength as seen in eq.2. Power dependence and laser exposure over time were studied in both nitrogen and oxygen atmosphere, to see how the heating due to laser intensity affects the samples.

4.2.1 Laser power dependence

Spectra resulting from different laser powers can be seen in fig.13 for OP1 and fig.14 for OP6, showing the expected intensity increase as the optical depth of the filters decreases. This data was then deconvoluted to obtain the integrated intensity of the Raman signal and the background fluorescence which can then be seen plotted against measured power in fig. 15 and 16. As stated in section 3.2 the power was measured by splitting the beam and measuring part of the beam, so the laser power experienced by the sample is linearly proportional to the measured power, however it is not equal to the measured power.

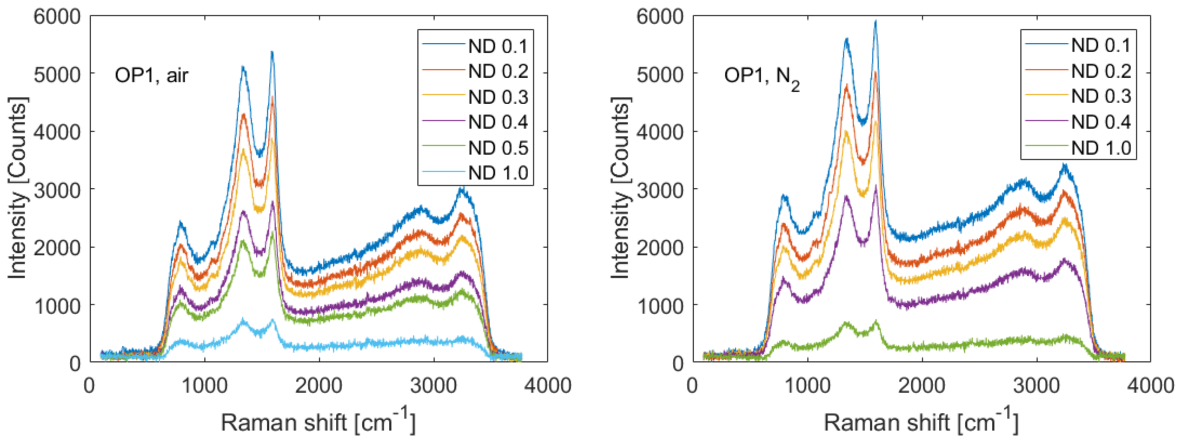

(a) *(b)*

Figure 13: *Raman spectra of OP1 obtained with different neutral density filters (ND) corresponding to different excitation power in air (a) and in nitrogen (b).*

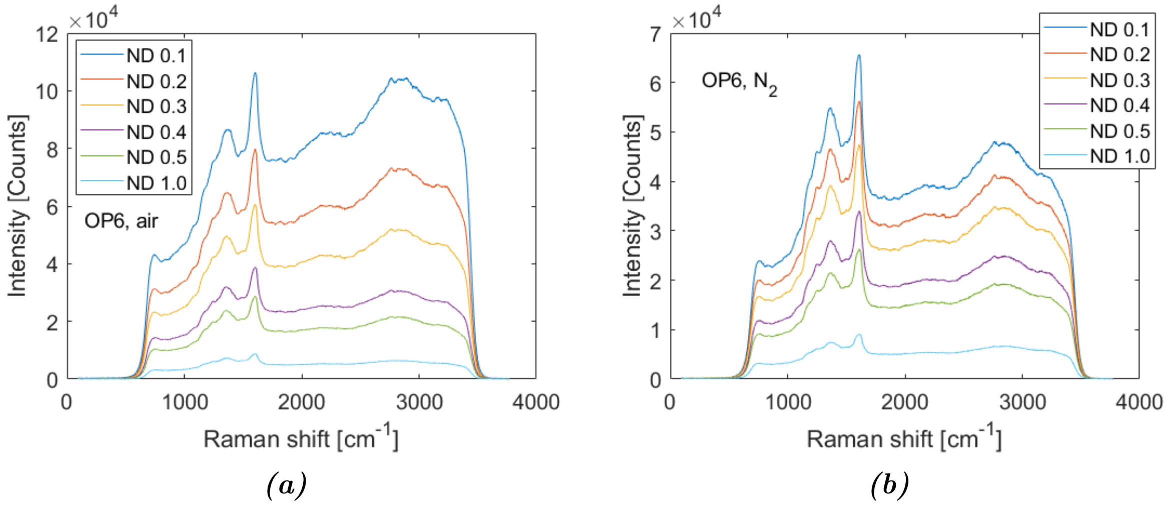

Figure 14: *Raman spectra of OP6 for different laser power in air (a) and in nitrogen (b).*

Each spectrum contains the first and second order Raman peaks of soot superimposed on a fluorescence background. The fluorescence of OP6 is much stronger than that of OP1. The fluorescence arises from a large fraction of organic carbon [15] including PAHs prevailing in such fuel rich flames [52, 53]. The fluorescence background thus depends on the hydrogen content, but it is not sensitive to hydrogen bonded to sp^2 bonded carbon [54].

As expected, the intensity dependence of the Raman signal is linearly increasing with power for OP1 in both air and nitrogen. There is a difference in intensity of the fluorescence between air and nitrogen measurements however, possibly due to the influence of the oxygen in the atmosphere interacting with the samples. As this is the mature soot, this effect can be explained by oxidation of reactive surface structures [55] containing hydrogen, caused by laser heating, and being evaporated in the process. The Raman signal is then unaffected as the structured carbon is less reactive than the organic compounds.

The peak in the range of 700-1000 cm^{-1} is a result of the sapphire substrate, the sapphire window in the lid of the Linkam and the ceramic heating element shown in fig.27 and 28. These features are seen for OP1 but is less prevalent for OP6 due to the increased Raman signal and fluorescence intensity for OP6. These contributions are both removed from the intensity integration by limiting the range of integration to the first and second order regions.

For the OP6 soot the fluorescence shows the opposite behavior compared to OP1 in terms of atmospheric influence. The power dependence is still linear for the Raman signal; however the intensity of fluorescence signal is increased in air. The fluorescence of OP6 in air is also possibly increasing at a nonlinear rate implying some interaction between the

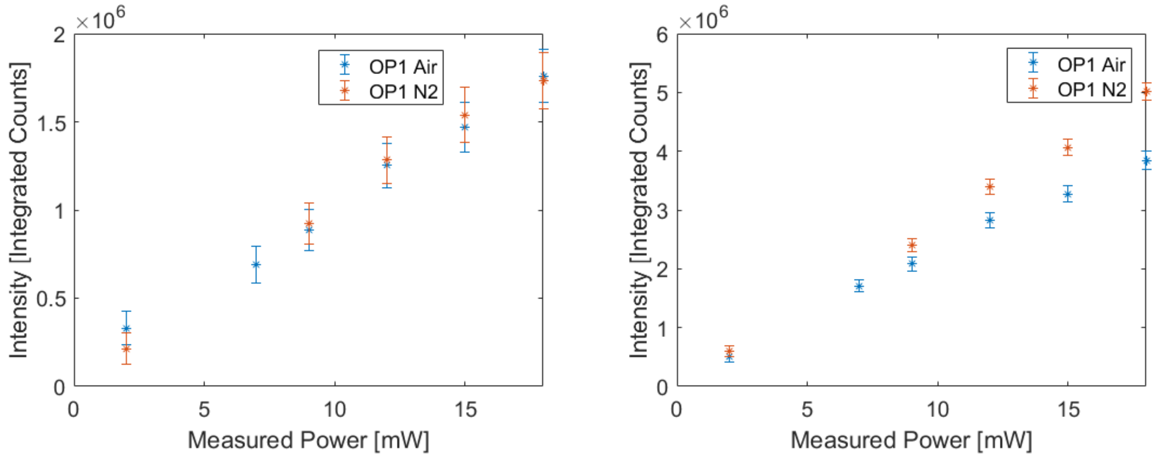

(a) *(b)*

Figure 15: *Integrated intensity of Raman signal (a) and fluorescence (b) for OP1 at different excitation laser power in air and in nitrogen. The signal intensity increases linearly with power as expected for the both Raman signal and the fluorescence.*

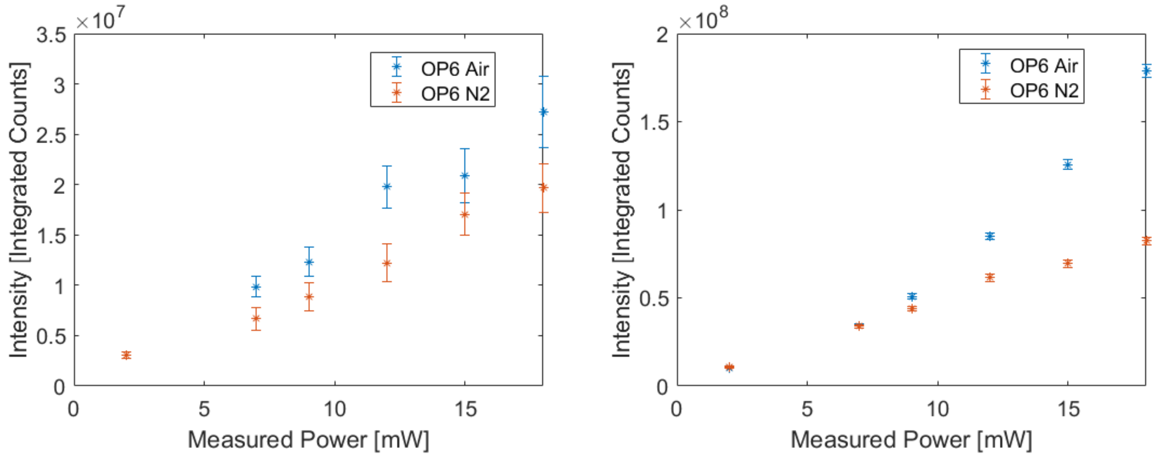

(a) *(b)*

Figure 16: *Integrated intensity of Raman signal (a) and fluorescence signal (b) for OP6 acquired with different neutral density filters in air and in nitrogen. The Raman signal intensity increases similarly to the same case for OP1, while the fluorescence of OP6 increases non-linearly in air.*

sample and the laser, however this is not definitive. This can be caused by an increase of soot probe volume, as the OP6 soot deposition onto the sapphire substrate is less than that of OP1. If this is the cause, the oxidation and subsequent evaporation of OP6 would, instead of reducing the background, result in laser induced fluorescence from the ceramic heating element which can be seen in fig.27. However, this is less likely, as the photoluminescence from the ceramic heating element would contribute a nonlinear background (with respect to wavenumber) and the fluorescence increase seen in the spectra does not follow the spectra of seen in fig.27. Another explanation is that the increase could be caused by a reaction between the soot and oxygen where the organic contents in the soot are oxidized but not evaporated, producing structures that have increased fluorescence output.

4.2.2 Laser radiation exposure

The effect of laser exposure over time can be observed in fig.17 and 18. The spectra of OP1 are primarily unchanged both in air and in nitrogen atmosphere except that the fluorescence intensity decreases by $\sim 10\%$. This reduction is most likely due to one of two things, evaporation of small amounts of volatile material or reduced laser intensity. The power of the laser was monitored throughout measurement, however the power resolution was on the order of mW, and the total signal decrease would correspond to a decrease of laser intensity of 1 mW. This is then possibly caused by a decrease in laser intensity, as the power reduction would be too small to detect. As the intensity of the Raman signal is not decreased as the fluorescence in fig.19, laser drift is less likely as the Raman signal intensity is linear with laser intensity and does not decrease in fig.19. This decrease is not observed in air however and so the laser power fluctuation is still a possible cause for the reduction in fluorescence of OP1 soot.

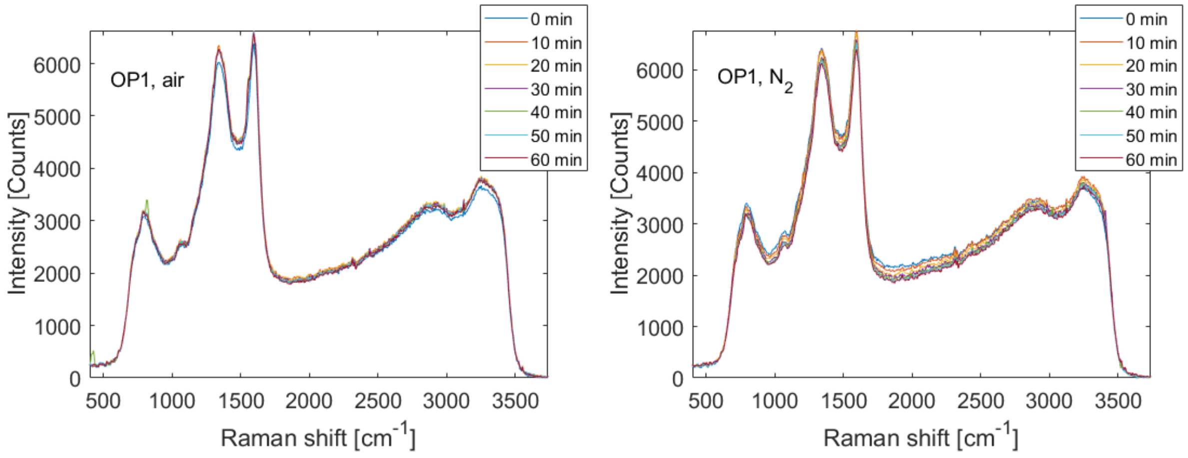

(a) ***(b)***

Figure 17: *Recorded Raman spectra of OP1 in air (a) and Nitrogen (b) for different exposure times.*

OP6 soot, the relatively disordered soot, is expected to be less stable due to a large fraction of organic components and the results are displayed in fig.18 and 20. There is a limited increase of intensity over time in nitrogen atmosphere, primarily in the fluorescence intensity which stabilizes after approximately 20 minutes. This is likely an effect of heating which is observed in the heating experiment series where the intensity increases with temperature if the sample is not oxidized or evaporated. In air however, the fluorescence drastically increases, and does so linearly with time for the range used here. As the Raman signal is not affected to the same extent, the primary explanation is that

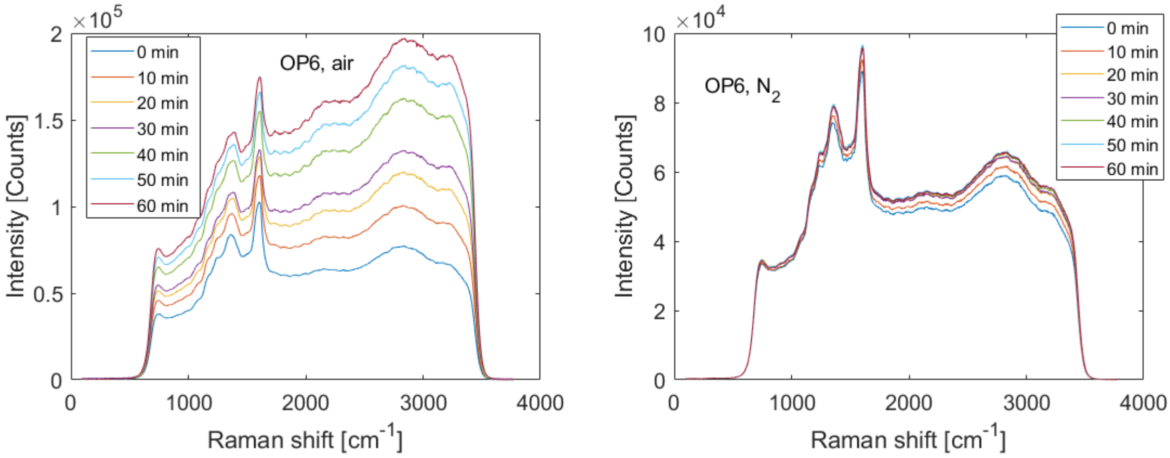

(a) *(b)*

Figure 18: *Recorded Raman spectra of OP6 in air (a) and Nitrogen (b) for different times exposed to laser radiation.*

surface PAHs and reactive components oxidize but are not evaporated. As the organic components of the soot react with oxygen, the amount of fluorescent material is increased and subsequently the fluorescence increases.

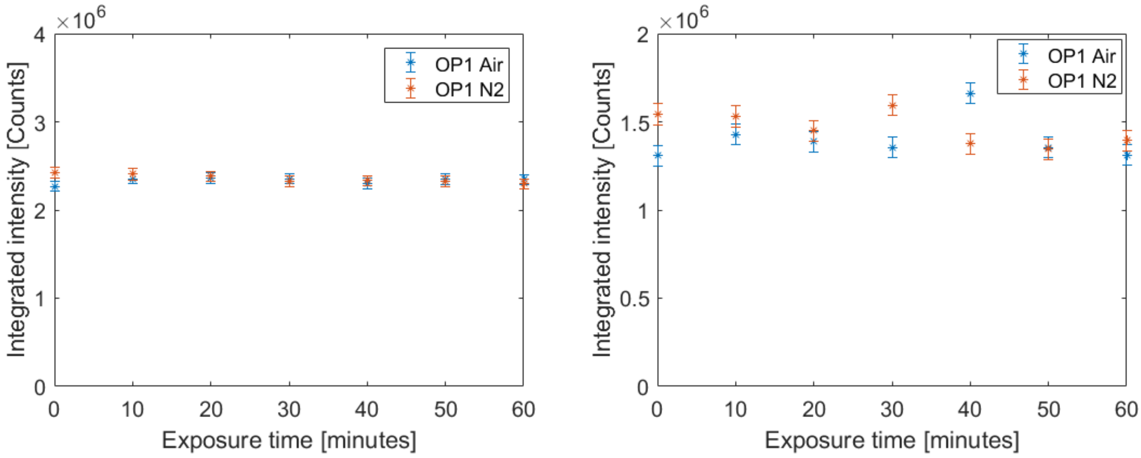

(a) *(b)*

Figure 19: *Integrated Raman signal (a) and fluorescence (b) intensity for OP1 as function of exposure time in air and nitrogen.*

4.2.3 Oxidation via heat treatment

The heating was performed with an air flow through the LINKAM heating stage and fig.21 show resulting spectra. The Raman spectra were recorded at room temperature, after heating the samples to the specified temperature and subsequently cooled.

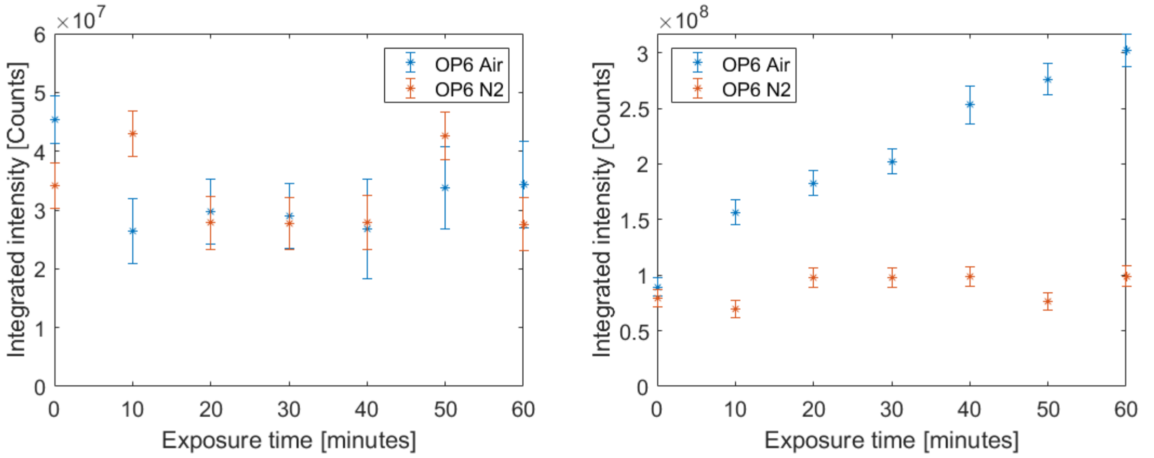

(a) *(b)*

Figure 20: *Integrated Raman signal (a) and fluorescence (b) intensity for OP6 as function of exposure time in air and nitrogen. The fluorescence signal increases linearly with exposure in air while is relatively unchanged in* N_2.

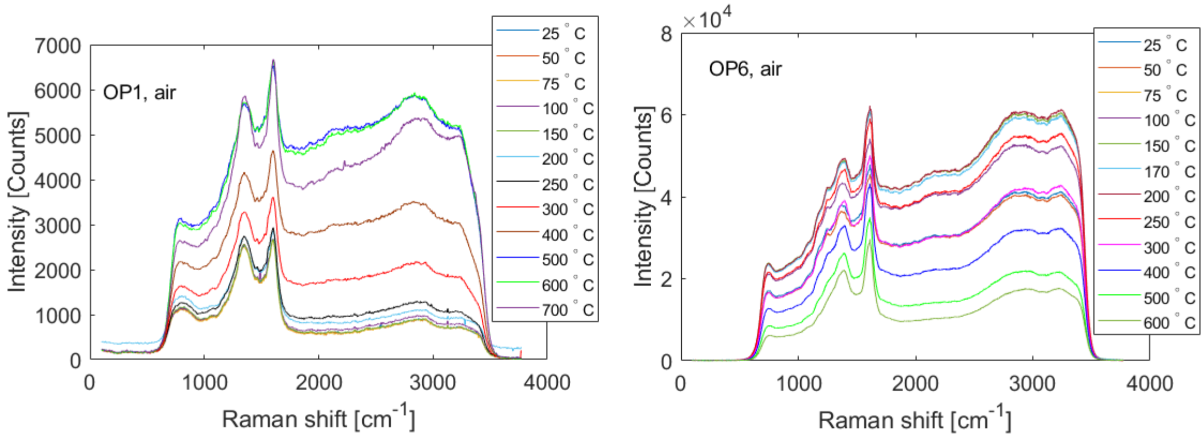

(a) *(b)*

Figure 21: *OP1 (a) and OP6 (b) Raman spectra after heating to specific temperatures. The overall intensity for OP1 increases at 200 °C however begins to decrease at temperatures above 400 °C. For OP6 the signal increases initially until 200 °C, where it decreases until complete evaporation.*

The heating experiment shows expected results in terms of stability. As OP1 soot has a more graphite-like structure, the stability is higher than that of OP6 soot which is represented in the rate the intensity of the Raman signal decreases above 500 °C and the temperature where the sample is completely evaporated. This finding is consistent with the soot oxidation study performed by Toth et al. [55] The Raman intensity increased for OP1 soot for higher temperatures, implying an increase in the Raman active material that is probed by the laser, which can be caused by conversion from amorphous carbon to ordered structures. Beyond this point however the soot is evaporated and no Raman signal is observed. The fluorescence of OP1 soot, as seen in fig.22, shows a strong increase

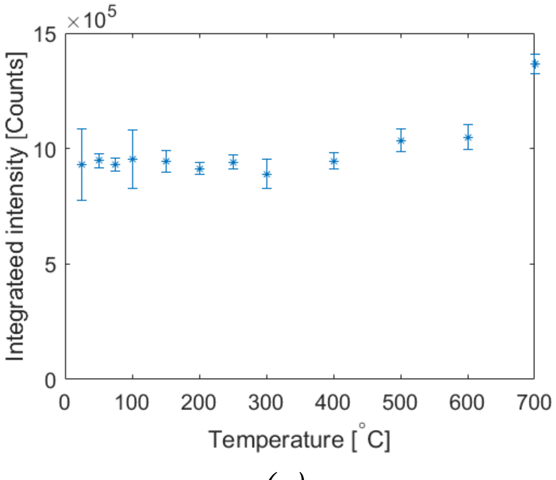

(a) ***(b)***

Figure 22: *Raman (a) and fluorescence (b) integrated intensity for OP1 after heating. Here an increase in Raman intensity is seen initially, followed by evaporation and oxidation at higher temperatures. At 700 °C the sample is evaporated entirely and the spectra observed is equivalent to that of the sapphire substrate and the ceramic heating element.*

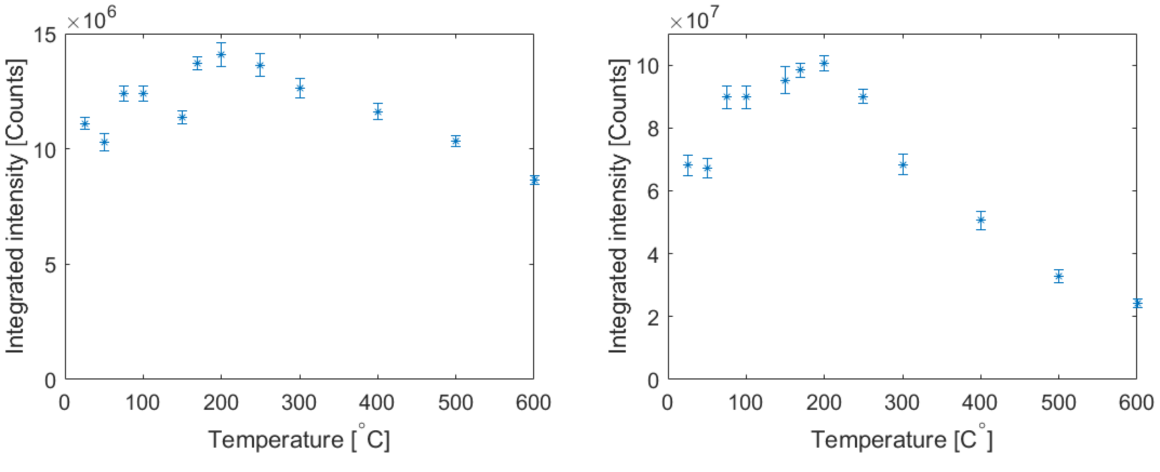

(a) ***(b)***

Figure 23: *Raman (a) and fluorescence (b) integrated intensity for OP6 after heating. For the OP6 sample the fluorescence intensity is initially stationary however it begins to decrease above 200 °C. The Raman intensity increases up to 200 °C and decreases with temperature above that. Complete evaporation of OP6 occurs at 600 °C.*

at temperatures above 200 °C as a result of possible oxidation of the soot which produces fluorescent compounds, or resulting from the quenching of the fluorescence signal in volatile materials [54].

A sinusoidal pattern is observed for OP6 spectra in several measurements, and the peak positions are linear with wavelength which implies that it is an interference effect caused by the setup which is noticeable for OP6 soot as the signal-to-noise ratio is larger for this sample. The shoulder peak of D_1 decreases for higher temperatures. This reflects a removal of volatile compounds due to oxidation and evaporation at a rate higher than that of the soot nucleus. The disappearance of this peak at high temperatures can be caused by increased structural order or that these compounds are evaporated.

4.2.4 Polarization dependence of Raman peaks of carbon black

Two carbon black samples were compared in term of polarization dependence, one of the non-heat-treated (CXN-550) and one annealed sample (INR-A) and their normalized spectra can be seen in fig .24 and 25 respectively.

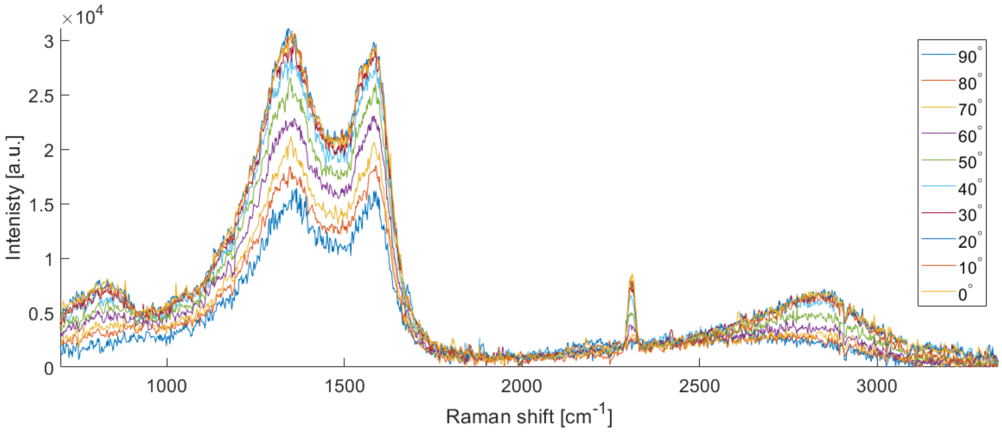

Figure 24: *Polarization dependent Raman spectra for CXN-550. The values shown in the legend are designated as the angular difference from that of the polarization of the incoming radiation. the first order decreases as expected and is not blocked out completely at any polarization. It can be observed that the second order is not affected homogeneously, as a broad intensity increase is present at approximately 2600 cm*$^{-1}$ *for all polarizations. This can be a component of the fluorescence that has not been fitted by the protocol.*

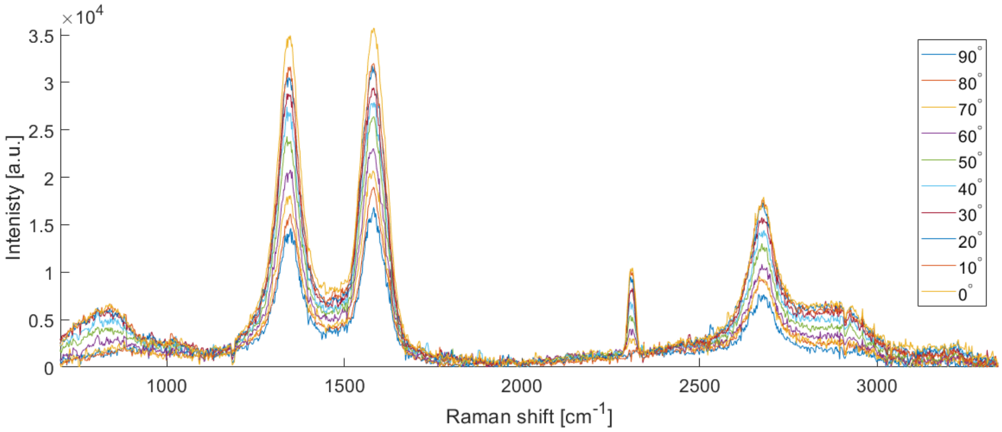

Figure 25: *Polarization dependent Raman spectra for INR-A. The decrease in intensity implies a depolarization ratio of approximately 0.5, similar to that of CXN-550. The broad peak at 900 cm*$^{-1}$ *is present and is observed to be highly polarized relative to the rest of the spectrum.*

As the polarization dependence of Raman scattering relates to the type of mode of vibration, different modes will have different depolarization ratios [34]. The G peak is a symmetric stretching mode that is expected to have a depolarization ratio close to 1 in ordered materials, meaning it is completely depolarized [47]. For amorphous carbons the depolarization ratio of the peaks will not be 1 however, as the lattice discontinuities produce non-uniform potentials, resulting in a non-unity depolarization ratio for peaks in materials such as graphene [56]. With increasing amorphous content, the depolarization ratio of other peaks should become similar to that of D_1. In section 4.1 it was discussed that INR-A is more ordered than CXN-550, and is expected to have a larger depolarization ratio for the G-peak and the second order. The nitrogen peak at 2330 cm^{-1} is seen in the spectra and has strong polarization dependence for comparison [34].

The calculated depolarization ratio of CXN-550 was 0.51 for both the G and D_1 peak, while for INR-A the ratios obtained were 0.45 and 0.40 for the G peak and D_1 peak. While the D_1 peak is less depolarized than G as expected for INR-A, the comparison between the CXN-550 and INR-A shows that the depolarization ratio of G is similar to the depolarization of D_1 however, it is larger for CXN-550. This is possibly caused by the increase in depolarization of D_1 with increasing structural order [57]. However, the second order shows a depolarization behavior that is expected, as the second order for CXN-550 is less depolarized than the second order of INR-A, relating to the depolarization of the $2D_1$ peak. The behavior of the band at ~826 cm^{-1} shows a strong polarization dependence, and has a depolarization ratio less than 0.1 for both samples, similar to that of nitrogen. This peak is possibly due to residual PAH based fuel that is adsorbed on the surface of the carbon black particles. The intensity of this peak is however stronger than expected of residual fuel which is expected to be less than 0.1% of the total mass [58].

4.3 Discussion regarding uncertainties in experiment and deconvolution

The different fitting protocols were tested in terms of goodness of fit values. Adjusted R-square was closest to 1 and normalized root mean square error (NRMSE, normalized by mean counts for each spectra) was lowest for a model including a BWF function G peak, Lorentzian functions for D_1, D_4, D_5, $2D_1$, $2D_2$, $2D_4$ and Gaussian functions for the 830 cm^{-1} and D+G peak.

In tab.4 the average adjusted R-squared and NRMSE of the protocols used to deconvolute the carbon black spectra are shown, averaged over all spectra seen in fig.9. The table shows that goodness of fit does not vary significantly between different models and

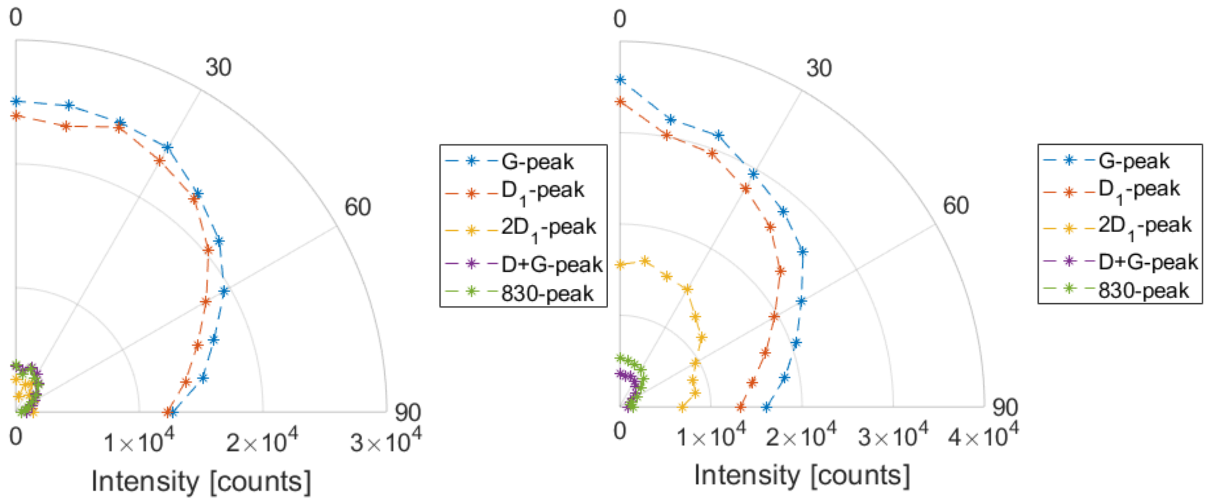

(a) *(b)*

Figure 26: *Polar plots of the peak intensities of CXN-550 (a) and INR-A (b) for different analyzer angles relative to the excitation polarization.*

Table 4: *The average NRMSE and adjusted R-square for different protocols, the table notations for the protocols is as following: [Peak type, number of peaks of type](Peaks), where peak type is Lorentzian (L), Gaussian (G) or Breit-Wigner-Fano (BWF).*

Protocol	average adj. Rsquare	average NRMSE
[L,5](G,D_1,D_3,D_4,D_5)	0.9943	0.0897
[L,4](G,D_1,D_4,D_5), [G,1](D_3)	0.9949	0.0861
[L,6](G,D_1,D_2,D_3,D_4,D_5)	0.9915	0.1121
[L,5](G,D_1,D_2,D_4,D_5), [G,1](D_3)	0.9957	0.0818
[BWF,1](G), [L,3](D_1,D_4,D_5)	0.9953	0.0938
[BWF,1](G), [L,1](D_1)	0.9938	0.1124

remains within 1% from an adjusted R-square of 1 for all protocols and the NRMSE is approximately 8-11% for the different protocols. Hence, it is not possible to decide which protocol provides the most accurate deconvolution of the data. However, using a BWF function for fitting the G peak has been motivated in literature [38, 43, 45], as structural disorder should couple the G-peak to a continuum of phonon density of states which results in an asymmetric shape. Increasing the number of parameters (in this case peaks) does generally lead to an increase in GoF, however this also results in a lack of consistency in resulting fits and must be physically motivated. As the BWF function has a theoretical motivation these protocols were chosen. For certain spectra, shoulders appeared on the

D_1 peak corresponding to D_4 and D_5 which could not be fitted by the last protocol in table 4. As a result of this the protocol used to treat the data was a BWF function for the G-peak and three Lorentizian functions for the first order.

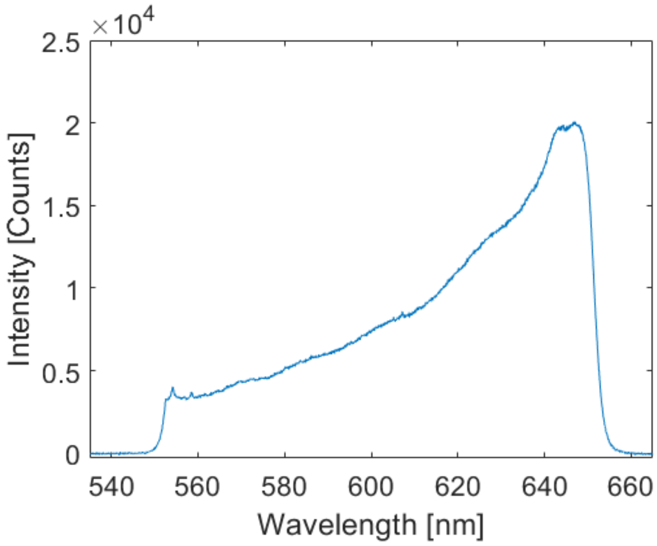

Figure 27: *Spectral contributions from ceramic heating element and sapphire substrate. The majority of the contribution is from the ceramic heating cup, while peaks around 550 nm are due to the sapphire substrate.*

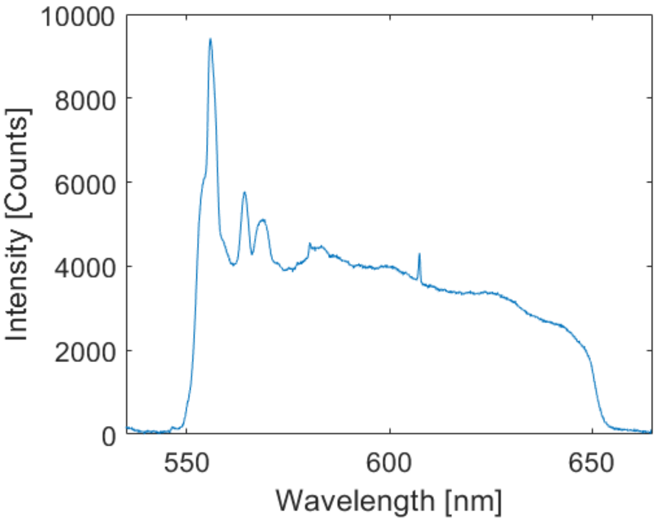

Figure 28: *The window of the Linkam lid produces a Raman spectra that is present in the measurements where the atmosphere is maintained throughout the acquisition, which are the heating, power dependence and laser exposure effects measurements.*

Components of the Linkam heating stage contribute to the spectra of all experiments performed with the Linkam. The spectral contributions from these can be seen in fig.27, 28 and 29. While the soot is deposited on the substrate, the spectral contributions from the heating element and substrate are small relative to the Raman signal. However, in the heating experiments the soot is evaporated at high temperatures which increases the transmitted laser light through the sample. As a result, the laser induced fluorescence of the ceramic cup dominates the spectra after heating the sample to temperatures above ∼600 °C and measuring Raman spectra at room temperature.

A broad peak can be seen at ∼550 nm (750 cm^{-1}) as a result of the window in spectra acquired through the window. These contributions originate from sapphire peaks that can be seen in fig.28. To avoid these peaks affecting the calculated integrated intensity the integration was performed for the range only including the Raman peaks of the soot.

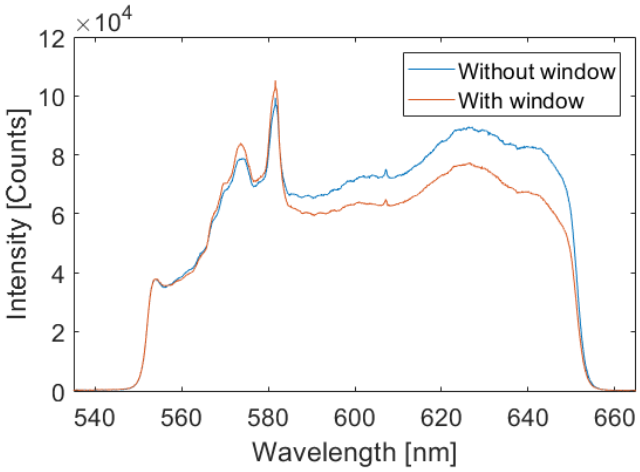

Figure 29: *Spectral changes due to the window can be seen here. The sample is OP6 in nitrogen and the effects of the window result in a reduction of the signal.*

The window affects the Raman and background signal of the spectra due to the transmission through the window which depends on wavelengths. This is accounted for in the spectra affected by this by calculating an intensity ratio for each pixel in two spectra seen in 29 and similar spectra for OP1. The intensity correction is then multiplied with the data in each spectrum.

5 Conclusions

Raman spectroscopy has been considered a very powerful tool to study structural information of carbonaceous materials for many decades [32, 38, 43, 45, 47]. However, there are still insufficient relations between spectral parameters and structural information of carbon based materials, particularly the polyaromatic unit size and the origin of some peaks [43, 45]. In addition, as far as we know there is no satisfactory knowledge about the impact of the measurement processes on the spectroscopic properties. The work performed here has led to interesting results on the missing points. The evolution of the spectral components under different conditions such as heating, laser polarization and manufacturing process have been studied in this report. Different measures of maturity were compared, with the primary method using the FWHM of the G peak in combination with the relative intensity of the D_1 and G peaks. The different samples used here were a set of six different carbon blacks and two types of soot produced by a miniCAST soot generator.

The mature miniCAST soot (OP1) shows a strong similarity to the carbon blacks that are not annealed post-flame, while the annealed carbon blacks have a structural order higher than that of soot. The carbon blacks that are not annealed produced similar Raman spectra. The FWHM_D and the ratio between the D_1 and G peak intensities showed that the annealed samples have a higher degree of structural order than both the soot samples and the other carbon blacks, while the carbon blacks that were not heat treated are structurally similar to the OP1 soot. OP1 soot in turn is showed to be more structurally ordered than OP6 soot. An estimation of the polycyclic aromatic unit length was performed for all samples, showing a trajectory of structural order for soot samples with L_a ranging from 1 to 6 nm. The compression process that had been performed on three carbon black samples did not show any significant effect in terms of Raman spectrum.

Possible links between surface area measures such as Iodine number and STSA and the Raman spectra were discussed and a possible correlation showed that an increase in L_a also increases STSA and iodine number. However, more samples are required for certain results and this could be studied further.

A study of the polarization dependence of the carbon black spectra showed that it did not follow expectations for the G-peak, possibly influenced by the depolarization ratio of other surrounding peaks. However, the second order spectra have a depolarization ratio which increases with increasing graphitization as expected. A peak was observed at a Raman shift of ~ 830 cm^{-1}, and the origin of this peak is unknown. This peak has a depolarization ratio close to 0, implying it has a polarization dependence similar to that of N_2 gas.

For soot samples it was showed that the laser used for Raman spectroscopy can influence the soot and less stable soot is more susceptible to this. Laser radiation exposure increased the intensity of fluorescence for the OP6 sample linearly with time. The OP1 soot was however not affected to the same extent. Raman signal intensity is linearly dependent on laser power as expected, however the fluorescence of OP6 soot seemingly increased more in air than in nitrogen, due to laser heating which caused interaction with the oxygen.

The heating of OP6 soot in air showed an increase in fluorescence and Raman signal for temperatures up to 200 °C, followed by a decrease and subsequent evaporation at temperatures above 600 °C. For OP1 soot the Raman signal remained stationary until temperatures of 500 °C while the fluorescence signal increased above 200 °C and the sample evaporated completely above 700 °C.

6 Outlook

Continuation of these experiments can follow different directions. The possible link between I_{D_1}/I_G and surface area estimate values of carbon black can be continued with a larger number of carbon black samples with a range of Iodine number and STSA. The comparison to annealed carbon blacks could also be performed to understand if this relation is affected by restructuring of the nano-scale structure as well. As the carbon blacks are expected to be stable at higher temperatures than soot, it could be interesting to monitor the annealing process using Raman spectroscopy which could not be performed in this work as the Linkam heating stage cannot be heated to temperatures required to anneal carbon black [12], which are generally stated to be above 1500 °C.

The evaluation of laser influence could be improved if transparency of soot with different maturity is taken into account. This is however difficult, as the collection method used for this work does not provide consistent deposition of soot. Evaluating the influence for a larger collection of soot produced at different operation points could also improve the understanding of these effects. The data collected to study the oxidation process can be studied further, specifically in terms of evolution of individual spectral features. The depolarization behavior of Raman peaks is relevant to understand their origin, and continuing this research for soot with different levels of structural order could provide an interesting view of how structural properties change throughout soot nucleation.

7 Acknowledgement

I would like to thank first and foremost my supervisors, Per-Erik and Cuong, for their help and teachings during the thesis work. As soot was a relatively new field for me, the work would have been significantly more difficult without their help. I would also like to thank the other members of the soot group, Sandra and Manu, for their input and discussions.

References

[1] H. A. Michelsen, Proceedings of the Combustion Institute **36**, 717 (2017).

[2] H. A. Michelsen, in Conference on lasers and electro-optics (2018), STh4L.1.

[3] T. C. Bond and R. W. Bergstrom, Aerosol Science and Technology **40**, 27 (2006).

[4] M. O. Andreae and A. Gelencsér, Atmospheric Chemistry and Physics **6**, 3131 (2006).

[5] M. R. Kholghy, A. Veshkini, and M. John Thomson, Carbon **100** (2016).

[6] E. Patterson and C. McMahon, Atmospheric Environment (1967) **18**, 2541 (1984).

[7] M. Lippmann, Critical Reviews in Toxicology **44**, 299 (2014).

[8] J. S. Lighty, J. M. Veranth, and A. F. Sarofim, Journal of the Air & Waste Management Association **50**, 1565 (2000).

[9] roberto_venturini CC BY-SA 3.0, `https://commons.wikimedia.org/wiki/File:Port-Saint-Louis-du-Rh%C3%B4ne_Navire_entrant_dans_le_port.jpg` (visited on 05/26/2019).

[10] S. Spalgais, D. Gothi, A. Jaiswal, and K. Gupta, Indian Journal of Occupational and Environmental Medicine **19**, 159 (2015).

[11] K. C. B.-S. 3.0, `https://commons.wikimedia.org/wiki/Category:All-Season_%26_All-Weather_tires#/media/File:All_Season_tire_tread_and_code.JPG` (visited on 05/26/2019).

[12] M. Pawlyta, J.-N. Rouzaud, and S. Duber, Carbon **84**, 479 (2015).

[13] H. Pierson, *Handbook of carbon, graphite, diamonds and fullerenes: processing, properties and applications*, Materials Science and Process Technology Series. Electronic (Elsevier Science, 2012).

[14] V. B. Malmborg, A. C. Eriksson, S. Török, Y. Zhang, K. Kling, J. Martinsson, E. C. Fortner, L. Gren, S. Kook, T. B. Onasch, P.-E. Bengtsson, and J. Pagels, Carbon **142**, 535 (2019).

[15] S. Török, V. Malmborg, J. Simonsson, A. Eriksson, J. Martinsson, M. Mannazhi, J. Pagels, and P. Bengtsson, Aerosol Science and Technology **52**, 757 (2018).

[16] J. Wu, L. Chen, P. Bengtsson, J. Zhou, J. Zhang, X. Wu, and K. Cen, English, Fuel **251**, 394 (2019).

[17] M. L. Botero, D. Chen, S. González-Calera, D. Jefferson, and M. Kraft, Carbon **96**, 459 (2016).

[18] P. Desgroux, X. Mercier, and K. A. Thomson, **34**, 1713 (2013).

[19] J. E. Elsila, N. P. de Leon, P. R. Buseck, and R. N. Zare, Geochimica et Cosmochimica Acta **69**, 1349 (2005).

[20] C. Mihesan, M. Ziskind, E. Therssen, P. Desgroux, and C. Focsa, Journal of Physics: Condensed Matter **20**, 025221 (2007).

[21] A. Tregrossi, R. Barbella, A. Ciajolo, and M. Alfé, Combustion Science and Technology **179**, 371 (2007).

[22] H. Michelsen, C. Schulz, G. Smallwood, and S. Will, Progress in Energy and Combustion Science **51**, 2 (2015).

[23] A. Eckbreth, *Laser diagnostics for combustion temperature and species* (Taylor & Francis, 1996).

[24] N.-E. Olofsson, J. Simonsson, S. Török, H. Bladh, and P.-E. Bengtsson, English, Applied Physics B **119**, 669 (2015).

[25] A. Sadezky, H. Muckenhuber, H. Grothe, R. Niessner, and U. Poschl, Carbon **43**, 1731 (2005).

[26] C. Russo and A. Ciajolo, Combustion and Flame **162**, 2431 (2015).

[27] C. Russo, F. Stanzione, M. Alfe, A. Ciajolo, and A. Tregrossi, Combustion Science and Technology **184**, 1219 (2012).

[28] H. Wang, Proceedings of the Combustion Institute **33**, 41 (2011).

[29] M. Frenklach, Phys. Chem. Chem. Phys. **4**, 2028 (2002).

[30] J.-B. Donnet, Carbon **32**, 1305 (1994).

[31] M. B. Vázquez-Santos, E. Geissler, K. László, J.-N. Rouzaud, A. Martínez-Alonso, and J. M. Tascón, Carbon **50**, 2929 (2012).

[32] J. Robertson and E. P. O'Reilly, Phys. Rev. B **35**, 2946 (1987).

[33] J. Simonsson, N.-E. Olofsson, S. Török, P.-E. Bengtsson, and H. Bladh, Applied Physics B **119**, 657 (2015).

[34] C. Banwell and E. McCash, *Fundamentals of molecular spectroscopy*, European Chemistry Series (McGraw-Hill, 1994).

[35] P. Sherwood and P. Sherwood, *Vibrational spectroscopy of solids*, Cambridge monographs in physical chemistry (Cambridge University Press, 1972).

[36] A. C. Ferrari, Solid State Communications **143**, Exploring graphene, 47 (2007).

[37] D. Yoon and H. Cheong, "Raman spectroscopy for characterization of graphene", in *Raman spectroscopy for nanomaterials characterization*, edited by C. S. S. R. Kumar (Springer Berlin Heidelberg, Berlin, Heidelberg, 2012), pp. 191–214.

[38] A. C. Ferrari and J. Robertson, Phys. Rev. B **64**, 075414 (2001).

[39] H. Ziari, A. Habibnejad Korayem, M. Hajiloo, M. Nakhaei, A. Razmjou, and H. Divandari, Construction and Building Materials **152**, 182 (2017).

[40] S. Raval, "Ultrafast pump-probe spectroscopy of graphene oxide (go) and reduced graphene oxide (rgo)", PhD thesis (Apr. 2018).

[41] B. Dippel, H. Jander, and J. Heintzenberg, Phys. Chem. Chem. Phys. **1**, 4707 (1999).

[42] C. Thomsen and S. Reich, Phys. Rev. Lett. **85**, 5214 (2000).

[43] N. Larouche and B. L. Stansfield, Carbon **48**, 620 (2010).

[44] M. Tommasini, D. Fazzi, A. Milani, M. Del Zoppo, C. Castiglioni, and G. Zerbi, The Journal of Physical Chemistry A **111**, PMID: 17941620, 11645 (2007).

[45] P. Mallet-Ladeira, P. Puech, C. Toulouse, M. Cazayous, N. Ratel-Ramond, P. Weisbecker, G. L. Vignoles, and M. Monthioux, Carbon **80**, 629 (2014).

[46] A. C. Ferrari and J. Robertson, Phys. Rev. B **61**, 14095 (2000).

[47] F. Tuinstra and J. L. Koenig, The Journal of Chemical Physics **53**, 1126 (1970).

[48] L. Cançado, A. Jorio, E. Martins Ferreira, F. Stavale, C. Achete, R. Capaz, M. Moutinho, A. Lombardo, T. Kulmala, and A. Ferrari, Nano letters **11**, 3190 (2011).

[49] G. A. Zickler, B. Smarsly, N. Gierlinger, H. Peterlik, and O. Paris, Carbon **44**, 3239 (2006).

[50] J. Robertson and E. P. O'Reilly, Phys. Rev. B **35**, 2946 (1987).

[51] *Linkam scientific instruments, ts1500, ts1200 and ts1000 systems*, `https://static1.squarespace.com/static/556d800ae4b0e8f91507450c/t/56d07abf40261db4d8f3f2da/1456503499575/TS1000_1200_1500_systems_v1.4.pdf` (visited on 04/26/2019).

[52] L. Mueller, G. Jakobi, J. Orasche, E. Karg, M. Sklorz, G. Abbaszade, B. Weggler, L. Jing, J. Schnelle-Kreis, and R. Zimmermann, Analytical and Bioanalytical Chemistry **407**, 5987 (2015).

[53] S. Bejaoui, X. Mercier, P. Desgroux, and E. Therssen, Combustion and Flame **161**, 2479 (2014).

[54] C. Pardanaud, C. Martin, P. Roubin, G. Giacometti, C. Hopf, T. Schwarz-Selinger, and W. Jacob, Diamond and Related Materials **34**, 100 (2013).

[55] P. Toth, D. Jacobsson, M. Ek, and H. Wiinikka, Carbon **145**, 149 (2019).

[56] M. Yoshikawa, N. Nagai, M. Matsuki, H. Fukuda, G. Katagiri, H. Ishida, A. Ishitani, and I. Nagai, Phys. Rev. B **46**, 7169 (1992).

[57] Y. Kawashima and G. Katagiri, Phys. Rev. B **59**, 62 (1999).

[58] R. Baan, K. Straif, Y. Grosse, B. Lauby-Secretan, F. Ghissassi, and V. Cogliano, The lancet oncology **7**, 295 (2006).